

Mobile-Cloud Inference for Collaborative Intelligence

by

Mateen Ulhaq

Thesis Submitted in Partial Fulfillment of the
Requirements for the Degree of
Bachelor of Applied Science (Honours)

in the
School of Engineering Science
Faculty of Applied Sciences

© **Mateen Ulhaq 2020**
SIMON FRASER UNIVERSITY
Spring 2020

Copyright in this work rests with the author. Please ensure that any reproduction or re-use is done in accordance with the relevant national copyright legislation.

Approval

Name: Mateen Ulhaq

Degree: Bachelor of Applied Science (Honours) (Engineering Physics)

Title: Mobile-Cloud Inference for Collaborative Intelligence

Examining Committee: Chair: **Dr. Ivan V. Bajić, P.Eng.**
Academic Supervisor
Professor

Dr. Mirza Faisal Beg, P.Eng.
Committee
Professor

Dr. Jie Liang, P.Eng.
Committee
Professor

Date Defended: June 9, 2020

Abstract

As AI applications for mobile devices become more prevalent, there is an increasing need for faster execution and lower energy consumption for deep learning model inference. Historically, the models run on mobile devices have been smaller and simpler in comparison to large state-of-the-art research models, which can only run on the cloud. However, cloud-only inference has drawbacks such as increased network bandwidth consumption and higher latency. In addition, cloud-only inference requires the input data (images, audio) to be fully transferred to the cloud, creating concerns about potential privacy breaches.

There is an alternative approach: shared mobile-cloud inference. Partial inference is performed on the mobile in order to reduce the dimensionality of the input data and arrive at a compact feature tensor, which is a latent space representation of the input signal. The feature tensor is then transmitted to the server for further inference. This strategy can reduce inference latency, energy consumption, and network bandwidth usage, as well as provide privacy protection, because the original signal never leaves the mobile. Further performance gain can be achieved by compressing the feature tensor before its transmission.

Acknowledgments

Firstly, I would like to thank my academic supervisor Dr. Ivan V. Bajić for his guidance, patience, and support. His feedback in reviewing and editing my thesis was invaluable. His experience and thoughtful ideas during meetings helped me navigate this new area of research. Furthermore, his encouragement motivated me to develop a prototype for demonstration at the NeurIPS 2019 conference.

I would also like to thank my committee members. Dr. Mirza Faisal Beg, who was my supervisor for a NSERC Undergraduate Student Research Awards (USRA) research project, and provided me with an opportunity to work on a challenging problem in computer vision, related to medical mobile applications. Dr. Jie Liang, who inspired and intrigued me with his lectures on Multimedia Communications Engineering involving the subjects of compression and deep learning.

The assistance my lab members Alon Harell and Hyomin Choi provided me during my demonstration at the NeurIPS 2019 conference was helpful in ensuring everything ran smoothly. Furthermore, their comments, along with those of Dr. Robert A. Cohen and Tim Woinoski, helped shaped the presentation of the demo and my thesis.

I would also like to show my appreciation for the community at SFU, including my friends and peers, as well as the professors of the schools of engineering science and computer science, and the departments of physics and mathematics.

And of course, for the neverending support from my family, including my mother and sister, I am grateful.

Contents

Approval	ii
Abstract	iii
Acknowledgements	iv
1 Introduction	1
1.1 On compressibility of deep features	3
1.2 Choosing where to cut a model	5
1.3 Thesis preview	7
2 Single tensor compression	9
2.1 Quantization	9
2.1.1 BatchNorm	9
2.1.2 Uniform quantization	11
2.1.3 Uniform quantization (per-neuron distribution)	13
2.2 Reusing image codecs	15
2.2.1 Tiling	15
2.2.2 JPEG	17
2.2.3 JPEG 2000	19
2.3 Summary	21
3 Towards tensor streams	22
3.1 Input transformations	22
3.2 Error concealment	26
3.3 Summary	27
4 Implementation	28
4.1 Prototype	28
4.1.1 NeurIPS demo	30
4.1.2 Inference pipeline	30
4.2 Latency model	33
4.3 Network protocol	36

4.4	Library	38
4.5	Summary	39
5	Conclusion	41
5.1	Thesis summary	41
5.2	Future work	42
5.2.1	Model architecture	42
5.2.2	Tensor compression	42
5.2.3	Error concealment	43
5.2.4	Network protocol	43
5.2.5	Libraries	43
	References	44
A	Additional figures	46

List of Figures

Figure 1.1	Comparison of inference strategies	2
Figure 1.2	Deep learning model as a graph	4
Figure 1.3	Layer inference latencies and output tensor sizes at cut points	6
Figure 1.4	Feature map of intermediate layer at different compression levels	8
Figure 2.1	BatchNorm histogram	10
Figure 2.2	Uniform quantization	12
Figure 2.3	Feature maps of quantized tensors	12
Figure 2.4	Mean and standard deviation feature maps	14
Figure 2.5	Uniform quantization (per-neuron distribution)	14
Figure 2.6	Feature map	16
Figure 2.7	JPEG accuracy vs compressed output size	18
Figure 2.8	JPEG 2000 accuracy vs compressed output size	20
Figure 3.1	Input translated	23
Figure 3.2	Input translated (subpixel)	25
Figure 3.3	Data loss accuracy	27
Figure 4.1	Android app	29

Figure 4.2	Demo at NeurIPS 2019	30
Figure 4.3	Full inference pipeline	32
Figure 4.4	Total inference latency vs bandwidth	34
Figure 4.5	Total inference latency vs bandwidth (actual)	35
Figure A.1	JPEG accuracy vs compressed output size (ResNet-34)	47
Figure A.2	JPEG 2000 accuracy vs compressed output size (ResNet-34)	49

Chapter 1

Introduction

Deep learning models have expanded the capabilities of mobile devices. Common applications include speech recognition, face recognition, pose estimation, object detection, night vision, artistic style transfer, and other image analysis and modification capabilities. However, more powerful and useful models also come with a significant computational load that takes time to run, and may be a drain on resources such as energy or the amount of available processing power for other computational tasks.

A client-only inference strategy, shown in Figure 1.1a, performs all processing on the client itself. In order to reduce the effect of the aforementioned negative factors on the mobile device, one may attempt to offload the computation by performing the complete inference on the server. This involves sending the input signal (e.g. images or audio) to the server over a network. This server-only inference strategy is visualized in Figure 1.1b. However, the amount of data sent to the server can consume large amounts of bandwidth, time, and energy, depending on the quality of the network connection. Also, sending images or audio directly to the cloud may raise privacy concerns.

This thesis considers a different approach: shared inference, also known as *collaborative intelligence* [1]–[3]. In an effort to reduce the inference latency and the amount of data sent over the network, the first part of the inference is performed on the client. The resulting intermediate tensor¹ is then compressed, serialized, and sent over the network. The server then reconstructs an approximation of the original tensor and completes the second part of the inference. The result can be transmitted back to the client and/or used for other analytics in the cloud. This is visualized in Figure 1.1c. In addition to possible energy savings and improved latency [1], [2], collaborative intelligence offers better possibilities for privacy protection because the original input signal never leaves the client device. What is transmitted to the cloud is the latent space representation of the input signal in the form of one or more deep feature tensors.

¹In machine learning and related fields, the word “tensor” is typically used to describe a multidimensional array. A tensor T can be *indexed* in the same way as an array. The number of indices required to reduce the tensor to a single number corresponds to its dimension. For instance, a vector is a 1-d tensor indexed by T_i ; a matrix is a 2-d tensor indexed by T_{ij} ; a “cube” of numbers is a 3-d tensor indexed by T_{ijk} ; and so on.

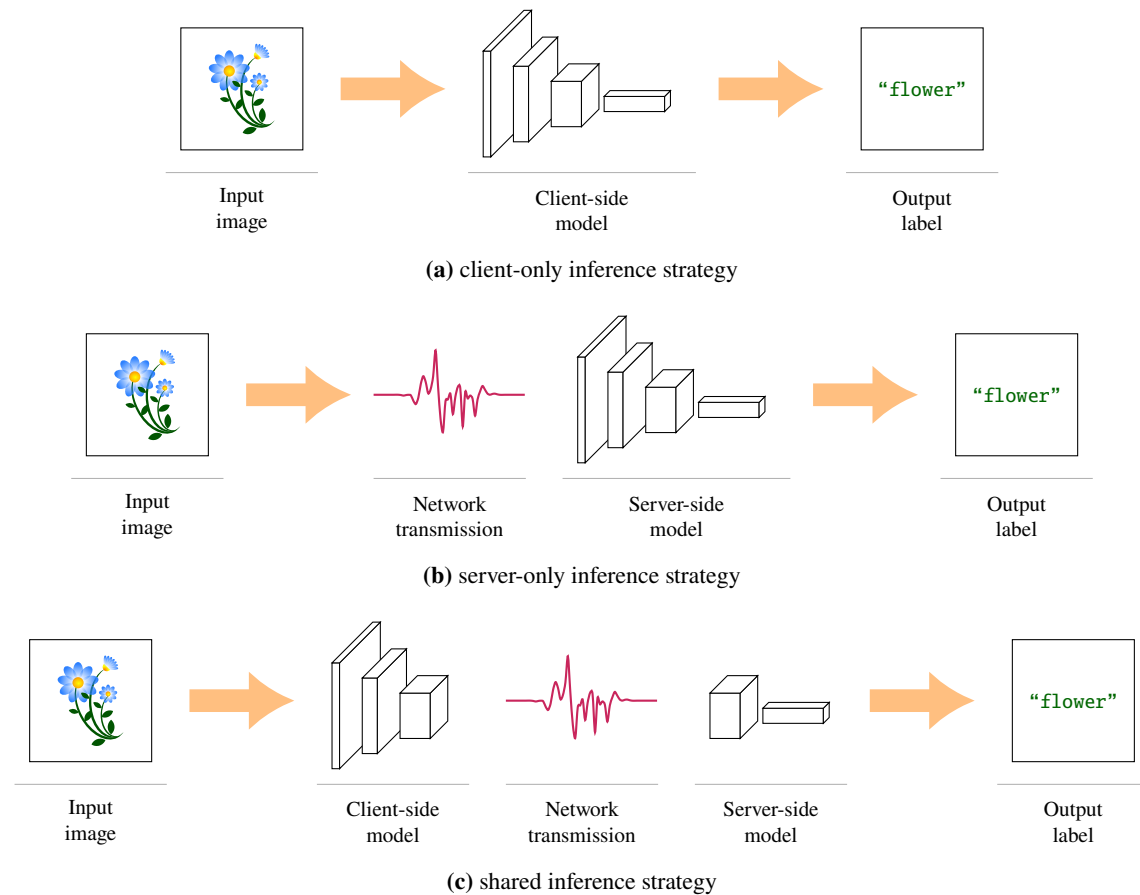


Figure 1.1: Comparison of inference strategies. (a) Client-only inference strategy. Advantages: no data is transmitted over the network. Disadvantages: client-side models may be limited in size and complexity, consume energy, or take up computational resources away from other tasks. (b) Server-only inference strategy. Advantages: ability to run heavier and more powerful models or multi-model. Disadvantages: may consume large amounts of bandwidth, susceptible to network latencies and instability, and privacy concerns from sending input data. (c) Shared inference strategy. The input image is first processed through the client-side model. The output of the client-side model is then serialized and transmitted over the network. The server receives the data, deserializes it, and then feeds it into the server-side model. Finally, the server-side model outputs the desired result. Advantages: allows for more computationally expensive inference models, potentially reduced bandwidth usage in comparison to server-only inference, and better privacy protection. Disadvantages: not suitable for all model architectures.

1.1 On compressibility of deep features

To motivate why collaborative intelligence may be feasible in terms of the amount of data that needs to be transferred to the server, it first helps to think about things from the point of view of information theory. By the *data processing inequality* [4], the mutual information between a signal and its processed version decreases as more and more processing is performed. Specifically, if X , Y , and Z are random variables (or vectors) and if $X \rightarrow Y \rightarrow Z$ is a Markov chain, then $I(X; Z) \leq I(X; Y)$. The inequality is non-strict, which means that mutual information need not decrease — it could stay the same. Data processing in a deep learning model with L layers may be formulated [5]–[7] as a Markov chain $X_1 \rightarrow X_2 \rightarrow \dots \rightarrow X_L$, where X_1 is the input, and X_l is the output of the l -th layer. Then, the data processing inequality implies that

$$I(X_1; X_2) \geq I(X_1; X_3) \geq \dots \geq I(X_1; X_L). \quad (1.1)$$

Thus, mutual information between the input X_1 and the outputs of successive layers is non-increasing.

The above reasoning only says that information *about the input* X_1 cannot increase as we move through the layers of a deep model; it does not say that the amount of information (i.e. the entropy) of X_l decreases as l increases. If we want to compress X_l , we need to examine the entropy of X_l , denoted $H(X_l)$. For this purpose, we recall another result from information theory [4]:

$$I(X_1; X_l) = H(X_l) - H(X_l | X_1). \quad (1.2)$$

The last term in (1.2) is the conditional entropy of l -th layer's output X_l given the input X_1 ; it is the uncertainty in the value of X_l , given X_1 . In non-generative feedforward neural networks, each layer's output is a deterministic function of the input. That is to say, when a given input X_1 is presented to the network, each layer's output is uniquely determined through feedforward propagation. There is no uncertainty in the value of X_l , given X_1 , and therefore $H(X_l | X_1) = 0$. Combined with the data processing inequality, this leads to the conclusion that in non-generative feedforward networks,

$$H(X_1) \geq H(X_2) \geq \dots \geq H(X_L). \quad (1.3)$$

Since the entropy is the limit of (lossless) compressibility [4], (1.3) predicts that the features taken from inside a non-generative feedforward network are at least as compressible as the input; and they become no less compressible as we move deeper into the network. This provides a theoretical basis for collaborative intelligence achieving the goal of sending less data to the server, compared to sending the input signal. Of course, this way of thinking merely provides theoretical bounds on information content and compressibility; it does not tell us how to construct a practical codec to achieve these limits.

More generally, consider a set of outputs of n layers in a deep non-generative model: $\{X_{j_1}, X_{j_2}, \dots, X_{j_n}\}$. These could be outputs of various layers in a single-stream model like

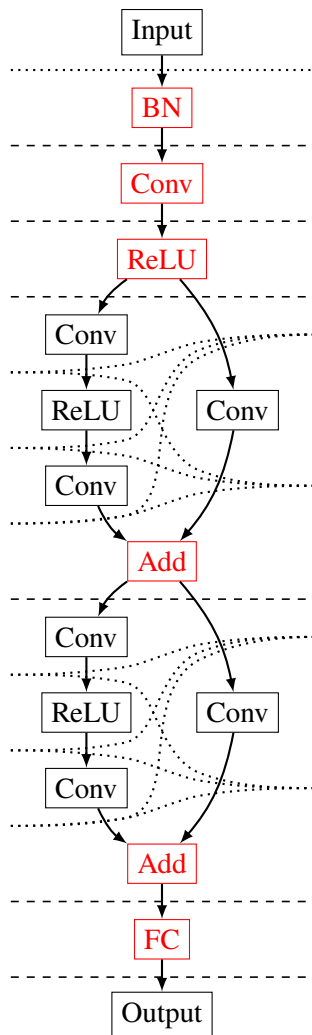


Figure 1.2: Deep model with both single-stream and multi-stream sections. Dashed and dotted lines show various possibilities for cutting the model. Cuts along dashed lines result in one feature tensor, those along dotted lines result in two feature tensors.

VGG16 [8], or a multi-stream model like U-Net [9]. Some models, such as ResNet [10], have both single-stream and multi-stream sections. A ResNet-like structure is shown in Figure 1.2 for illustration.

Let $Y = (X_{j_1}, X_{j_2}, \dots, X_{j_n})$ be their joint output. Note that Y is a deterministic function of the input X_1 — when X_1 is given, Y is uniquely determined, hence $H(Y | X_1) = 0$. By considering the Markov chain $X_1 \rightarrow X_1 \rightarrow Y$ and using the data processing inequality, we can write

$$\begin{aligned}
 H(X_1) &= I(X_1; X_1) \geq I(X_1; Y) \\
 &= H(Y) - H(Y | X_1) \\
 &= H(Y) \\
 &= H(X_{j_1}, X_{j_2}, \dots, X_{j_n}).
 \end{aligned} \tag{1.4}$$

Hence, the joint entropy of the outputs of n layers in a non-generative model is no larger than the entropy of the input. According to this result, in the limit, we should be able to compress (at least losslessly) outputs from any number of internal layers of a non-generative model, so long as we do it jointly. Again, as with the result in (1.3), this is a statement about limits of compression performance; it does not tell us how to actually construct such a joint codec.

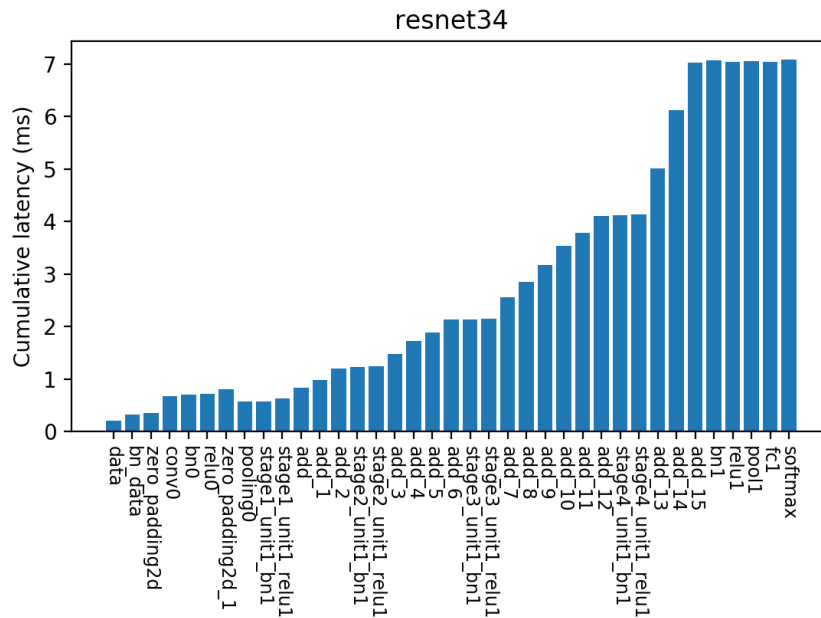
The above discussion applies to lossless compression of input and deep feature tensors. Analogous results for lossy compression are yet to be obtained, however, we believe that these also hold because in non-generative models, all layer outputs are uniquely determined once the input is presented to the model. The work presented in this thesis focuses on single-stream cuts, where one input produces a single tensor at the cut point. We study the performance of practical lossy compression for such scenarios.

1.2 Choosing where to cut a model

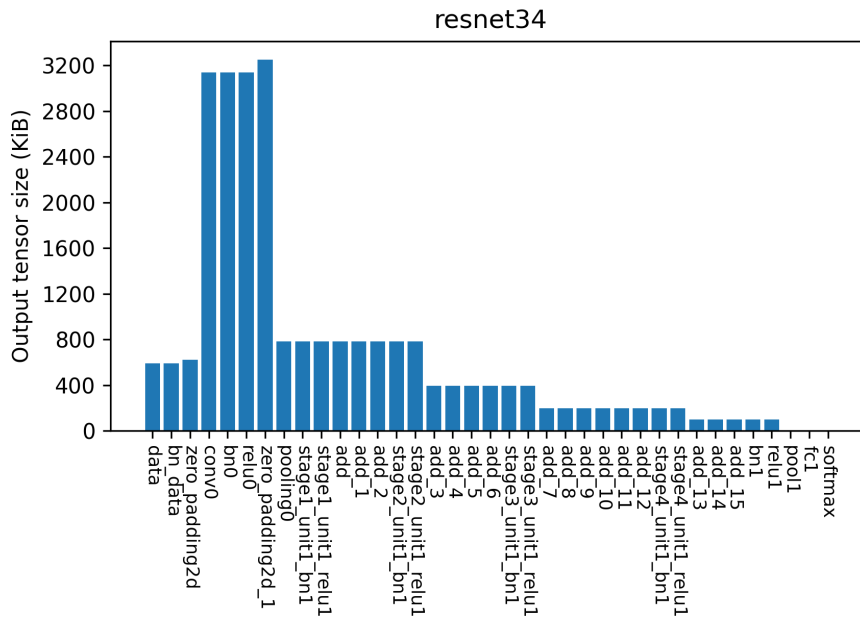
The best point to split a model at depends on a variety of factors. Selection of the best cut point has been studied by several research groups. In [1], the authors empirically select the cut points of various deep models based on measuring energy consumption at the mobile device and/or end-to-end latency. Their results indicate that the best cut point depends on the type of connectivity between the mobile and the cloud. If the mobile is connected via a Wi-Fi connection (high-bitrate, close to access point), the optimal cut point tends to be closer to the input, sometimes the input itself (i.e. sending the input signal directly). For cellular connections such as 3G or LTE (lower bitrate, far from access point), the optimal cut point is deeper in the model. The primary reason is that deeper cut points result in smaller data volumes, which results in less energy being used for the radio. Another study [2] presents a more comprehensive model of resource utilization in collaborative intelligence, which allows cut points to be selected by considering not only energy utilization at the mobile and end-to-end latency, but also cloud congestion and Quality of Service (QoS).

Consider Figure 1.3a, which plots the cumulative computation time² at various cut points, ordered in distance from the source. As expected, the cumulative computation time at cut points is monotonically increasing. By splitting the model at as early a cut point as possible, we can keep the amount of computation performed by the client-side model as small as possible and offload the rest of the computation to the server. However, if the split is performed too early in the model, the amount of information contained in the signal may remain too large to compress effectively. The output tensor sizes plotted in Figure 1.3b provide an upper bound on the compressed tensor sizes. Thus, models best suited towards a shared inference strategy are those that have a small computational footprint and reduce the input dimensions significantly in the early layers. Of course, due to the possibility of compression, these factors merely provide a rough guide.

²The cumulative computation time at a particular cut point refers to the amount of time it takes for inference to complete from the input to the cut point.



(a) cumulative inference latencies



(b) output tensor sizes

Figure 1.3: Layer inference latencies and output tensor sizes of ResNet-34 at cut points. The cumulative inference latencies were determined by running inference on the model up until the given cut point on an NVIDIA GeForce GTX Titan X. Note that the cumulative inference latencies are not necessarily monotonically increasing as we move deeper into the model; this is likely due to the reduced cost of copying tensors to output nodes (e.g. to a separate VRAM buffer) as their sizes decrease. The transfer latency between GPU and CPU (or rather, VRAM and RAM) is not included here.

The output tensors of intermediate layers of convolutional neural networks (CNNs) can often have structural redundancies between channels, which can be exploited for heavy compression. Consider Figure 1.4, which shows a tiled layout of the channels within the intermediate layer of a CNN. Within a given channel, nearby pixels often have similar intensity values. Furthermore, there also exist structural similarities across channels. These properties of local similarity and inter-channel similarity can be exploited to compress the data.

One also needs to consider how the compression scheme affects the model’s overall inference accuracy. While lossless compression is possible, it is often not very practical. Thus, we will be looking at lossy compression schemes that result in imperfect reconstructions of the intermediate signal, which can have an effect on the model’s accuracy.

In many applications, one is often performing inference on a series of inputs. These inputs often share structural similarities with each other. For instance, a series of frames taken from a video often have temporal redundancies that are exploited by video codecs. Thus, it is useful to also produce compression schemes for tensor “streams”. One desirable property of the input tensor for such a compression scheme is the stability of the tensor values with respect to minor changes in the input. For example, it is desirable that a small translation of the input image should result in a small recognizable change in the output tensor.

To summarize, when choosing which cut point to split the model at, one needs to make the following considerations:

- Is there a good split point that can be chosen as close to the input as possible, to minimize the cumulative computation from preceding layers?
- How compressible is the split layer’s output tensor data?
- How is inference accuracy affected by the lossy compression scheme applied to the split layer’s output tensor data?
- How stable is the split layer’s tensor output data with respect to minor changes in input data?

1.3 Thesis preview

In this thesis, we will look at developing tensor compression techniques, improving them, and also consider the challenges in developing a working implementation of collaborative intelligence. In Chapter 2, we will begin developing compression techniques for tensor data while attempting to maintain a good overall inference accuracy. Chapter 3 will demonstrate useful properties that can be used to develop better compression of tensor streams as well as the handling of missing or corrupted tensor data. Finally, in Chapter 4, we will discuss a proof-of-concept Android and server implementation for shared inference that was demonstrated at the NeurIPS 2019 conference [11]; we will also discuss other challenges that come up in creating real working implementations of collaborative intelligence and what can be done to resolve them.

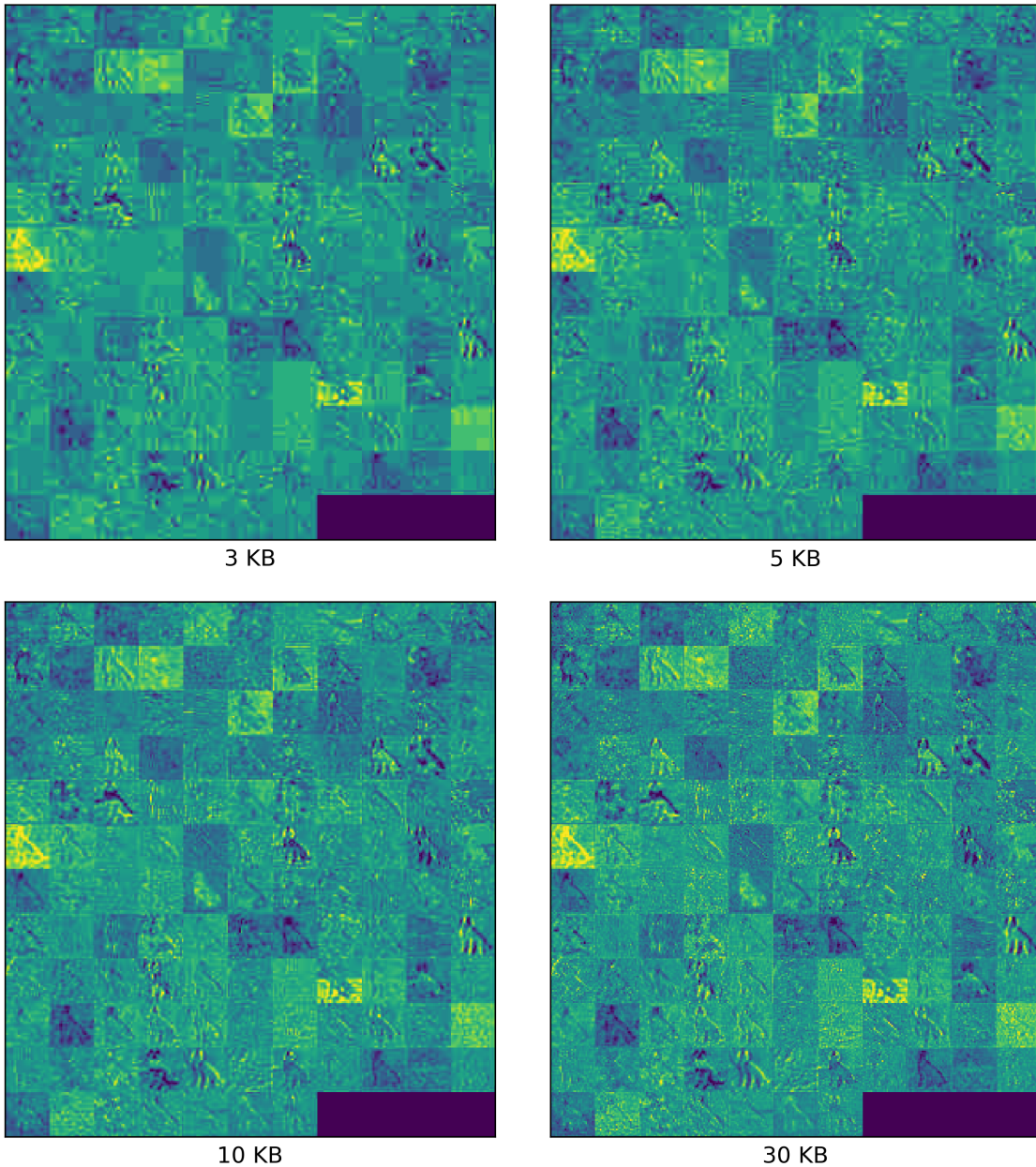


Figure 1.4: Feature map of intermediate `add_3` layer of ResNet-34 compressed to different sizes. The tensor of shape (h, w, c) is uniformly quantized to 8-bits, then tiled into a grid of (h, w) shaped channels. Different levels of JPEG compression are applied to the resulting “image”. Shown here are JPEGs of size 3, 5, 10, and 30 KiB. (The last of these is visually identical to the original tensor “image”.) The preceding layers within the network consist of conv2d layers, pooling layers, BatchNorm layers, addition layers, and ReLU activation layers. Because of this, some characteristics of the original image are still visually apparent within the individual channels (e.g. the outline of a dog). There are also inter-channel similarities. For example, one can classify the channels as “light”, “dark”, “noisy”, “smooth”, or some combination thereof. These inter-channel similarities can be exploited for better compression.

Chapter 2

Single tensor compression

One of the primary determinants for feasibility of the shared inference strategy is the amount of data transmitted over the network. The less data that is transmitted, the better the shared inference strategy performs in comparison to the server-only inference strategy. Common sources of input data such as images, video, and audio often have mature codecs that offer reasonable amounts of compression at low computational cost (albeit, with some privacy concerns). In order to be a competitive alternative to server-only inference, a shared inference strategy needs to be on par or outperform compression of input data. Thus, a major topic for mobile-cloud shared inference is the compression of intermediate tensor data. It is important to keep in mind that the primary objective is achieving good *inference accuracy* rather than reducing reconstruction error, though these goals often do coincide.

In this chapter, we will be investigating layer properties, quantization methods, and techniques for single tensor compression. First, we will see that models with BatchNorm layers often provide good candidate layers to split upon due to the light-tailed shape of their output distributions. Upon the output of these layers, we will apply quantization with varying levels and bins, and see how this affects the final inference accuracy. Then, we will look at specific methods for compressing single tensors from CNNs, for which we will utilize existing codecs such as JPEG and JPEG 2000.

2.1 Quantization

A first step towards good compression is quantization of the floating-point values of the tensor data. Though lossless compression of floating-point values themselves is possible, much of the precision they provide often does not affect accuracy significantly. Indeed, as we will soon see, one may sometimes get away with as few as 2 bits of precision per tensor element.

2.1.1 BatchNorm

Many models contain BatchNorm [12] layers to assist in training. It is a popularly held belief that training is sped up due to the reduction of Internal Covariate Shift (ICS) that occurs at a deep layer as a result of changing the parameters of earlier layers; however, this has been shown to be false [13]. Nonetheless, BatchNorm layers do appear to help limit the possible range of neuron output values

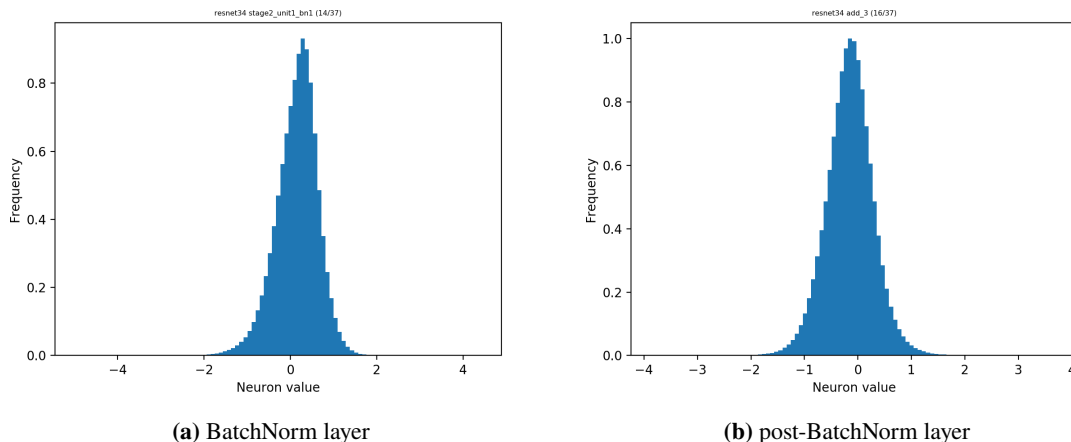


Figure 2.1: Histograms of neuron output values at various layers. (a) `stage2_unit1_bn1` (BatchNorm layer) of ResNet-34 with $\mu = 0.13, \sigma = 0.50$. (b) `add_7` (post-BatchNorm layer) of ResNet-34 with $\mu = -0.16, \sigma = 0.47$.

by “normalizing” the values by their standard deviation within mini-batches. By keeping a running average of the mean and variance, the estimated mean and variance also apply to a larger variety of inputs.

The BatchNorm equations are reproduced as follows [12]:

$$\mu_B = \frac{1}{m} \sum_{i=1}^m x_i \quad (2.1)$$

$$\sigma_B^2 = \frac{1}{m} \sum_{i=1}^m (x_i - \mu_B)^2 \quad (2.2)$$

$$\hat{x}_i = \frac{x_i - \mu_B}{\sqrt{\sigma_B^2 + \epsilon}} \quad (2.3)$$

$$y_i = \text{BN}_{\gamma, \beta}(x_i) = \gamma \hat{x}_i + \beta \quad (2.4)$$

where B refers to a mini-batch of size m , and γ and β are trainable parameters.

For ResNet models, the neuron output values of the BatchNorm layers *experimentally* appear to be approximately normally distributed with their own mean and standard deviation. Thus, we assume that the random variable associated with a single neuron output y_i is $Y_i \sim \mathcal{N}(\mu_i, \sigma_i^2)$. Additionally, the mixture distribution of neuron output values (which we take to be the mean average of the individual neuron output distributions) also *experimentally* appears to be roughly normally distributed: $Y \sim \frac{1}{n} \sum_{i=1}^n \mathcal{N}(\mu_i, \sigma_i^2) \approx \mathcal{N}(\mu, \sigma^2)$, where n is the total number of neurons in the layer. This is shown in Figure 2.1a for a layer from ResNet-34. Note that these are not mathematical facts and need not hold for all models and layers.

Sometimes, the distribution of neuron output values for layers that follow BatchNorm layers also *experimentally* appear to be normally distributed. This is the case for the layer visualized in

Figure 2.1b. Note that this isn't always the case: for example, a ReLU layer will clip negative values in the left tail of the distribution, making the resulting distribution non-normal. For a normal random variable, 99.7% of values lie within 3 standard deviations from the mean, so the tensor values can be clipped to the interval $[\mu - 3\sigma, \mu + 3\sigma]$ without significantly inaccurate reconstruction of too many values.

2.1.2 Uniform quantization

Uniform quantization involves constructing N evenly sized bins $B = \{(x_0, x_1], \dots, (x_{N-1}, x_N]\}$ over a finite interval $[x_{\min}, x_{\max}]$ and using a value between the bin edges as the reconstruction value for that bin. The number of bins is also known as the number of *levels* [14]. In the following experiments, we will use the midpoints of the bin edges as reconstruction values.

The process of quantization and dequantization is lossy; there is some error in reconstruction. A good choice for the number of levels and clipping interval will minimize the amount of distortion due to the imprecise reconstruction. The specific choice is dependent on the output distribution at the given layer.

Consider the distribution for the `add_3` layer of ResNet-34 shown in Figure 2.1b. Assuming normal distribution, 99.7% of possible neuron output values are contained within the interval $[\mu - 3\sigma, \mu + 3\sigma]$. Quantizing 32-bit float values over this interval to 256 levels (8-bits) gives us a compression ratio of 4:1 even without variable-length coding. A drop of $< 0.5\%$ in top-1 accuracy is measured by testing over 16,384 square-cropped images from the ILSVRC 2012 (ImageNet, 1000 classes) dataset [15], resized to 224×224 .

We can further improve on this by imposing the constraint $\mu = \frac{1}{2}(x_{\min} + x_{\max})$ (which fixes the center of the clipping interval to the mean value). Define the clipping width w by $[x_{\min}, x_{\max}] = [\mu - w\sigma, \mu + w\sigma]$. Then, we can choose the clipping width and levels experimentally by plotting the accuracy versus these two variables. This is done in Figure 2.2, for 16,384 input samples from the same dataset as above. Thus, we can achieve an accuracy drop of $< 0.5\%$ and a compression ratio of 11:1 (without variable-length coding) by quantizing to 7 levels (2.8 bits/tensor element) over the interval $[\mu - 3.3\sigma, \mu + 3.3\sigma]$. Because the distribution of neuron output values is roughly symmetric about the mean, it is unlikely that we can achieve significantly better results by expanding the interval. The feature map of an example tensor quantized using this method is shown in Figure 2.3a.

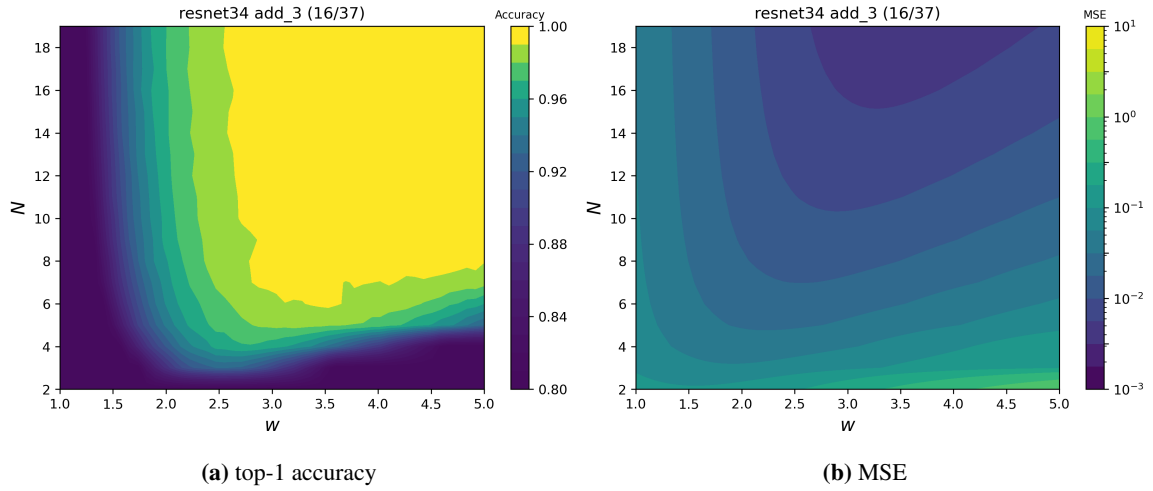


Figure 2.2: Analysis of uniform quantization scheme with N quantization levels and clipping range $[\mu - w\sigma, \mu + w\sigma]$, where w is the clipping width (in units of σ). (a) Plot of inference accuracy of the reconstructed tensor resulting from quantization and dequantization of intermediate tensor. Accuracy is scaled relative to baseline accuracy computed from regular model inference on the given dataset. The darkest color represents $\leq 80\%$ accuracy. (b) Plot of MSE between the original tensor and the reconstructed tensor.

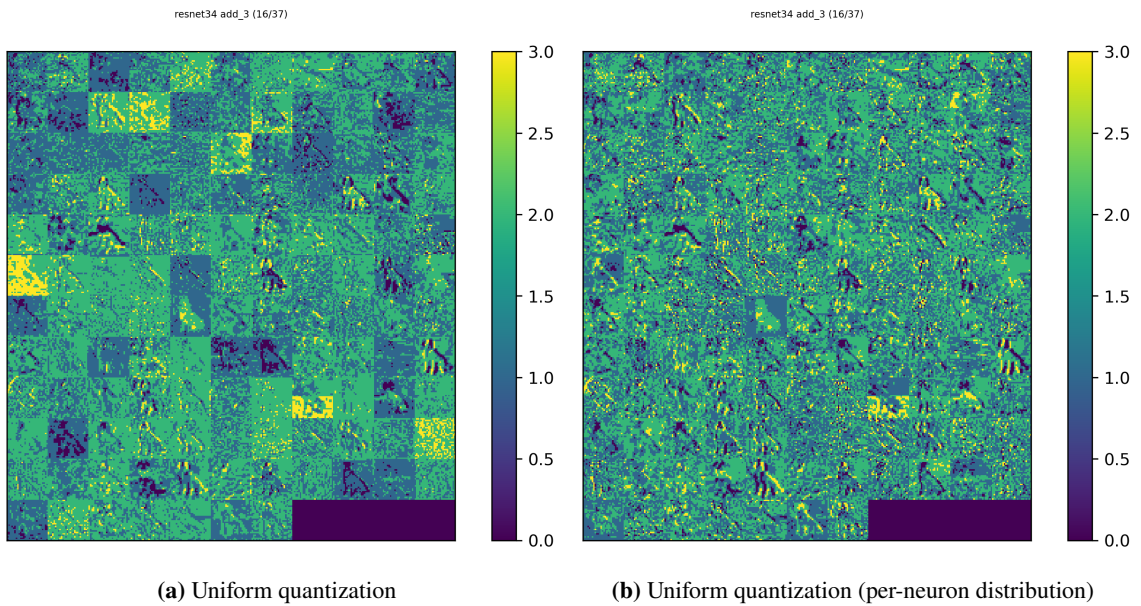


Figure 2.3: Feature maps of tensor data quantized by (a) uniform quantization with 4 levels over $[\mu - 3\sigma, \mu + 3\sigma]$ and (b) uniform quantization with 4 levels of neuron outputs normalized by their estimated distribution Y_i over the interval $[\mu_i - 3\sigma_i, \mu_i + 3\sigma_i]$.

2.1.3 Uniform quantization (per-neuron distribution)

While treating a neuron output as a normal random variable from the aggregate distribution shown in Figure 2.1b provides a good set of quantization bins, we can do better. Recognize that the output y_i of a single neuron has its own probability distribution. We may measure its characteristics with the typical estimators of mean $\mu_i = \mathbb{E}[Y_i]$ and variance $\sigma_i^2 = \mathbb{E}[(Y_i - \mu_i)^2]$. Figure 2.4 shows the mean and standard deviations computed individually for each neuron output, over 4096 sample images from the ILSVRC 2012 dataset.

Let $U = (N, I)$ be a uniform quantization strategy, where N is the number of levels and $I = [x_{\min}, x_{\max}]$ represents the clipping interval. In Section 2.1.2, we were quantizing each neuron output y_i using a single uniform quantization strategy U based on the aggregate distribution associated with Y . We will now quantize each neuron output y_i individually by a uniform quantization strategy $U_i = (N_i, I_i)$, based on the measured¹ probability distribution associated with Y_i .

Consider again the `add_3` layer of ResNet-34. We impose the constraint $\mu_i = \frac{1}{2}(x_{\min_i} + x_{\max_i})$ and define the clipping width w_i by $I_i = [x_{\min_i}, x_{\max_i}] = [\mu_i - w_i\sigma_i, \mu_i + w_i\sigma_i]$. To reduce the space of possible quantization strategies, we fix the number of levels to a single number, $N_i = N$. Furthermore, we also fix the clipping widths to a single number, $w_i = w$. The feature map of an example tensor quantized using this method is shown in Figure 2.3b. The accuracy of inference on the reconstructed tensor and the MSE of reconstruction versus N and w are plotted in Figure 2.5. In comparison to Figure 2.2, the MSE is lower. Furthermore, it takes fewer quantization levels (and thus, bits) to obtain a $< 0.5\%$ drop in accuracy, and a smaller clipping width. Thus, we can achieve an accuracy drop of $< 0.5\%$ and a compression ratio of 12:1 (without variable-length coding) by quantizing to 6 levels (2.6 bits/tensor element) over the interval $[\mu - 3.7\sigma, \mu + 3.7\sigma]$.

¹In the typical, non-measure-theoretic sense of the word.

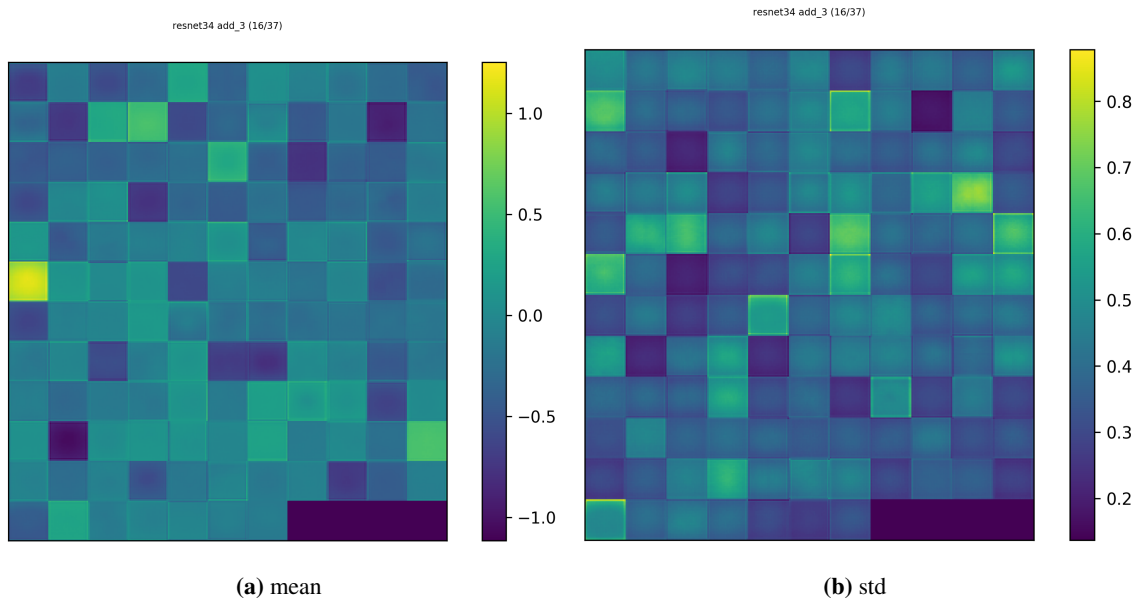


Figure 2.4: The tensors resulting from 16384 different inputs were used to determine each neuron output’s mean and standard deviation. The mean appears to be roughly the same for all neuron outputs within a given channel. The standard deviation is also roughly the same within each channel, though with some more variation.

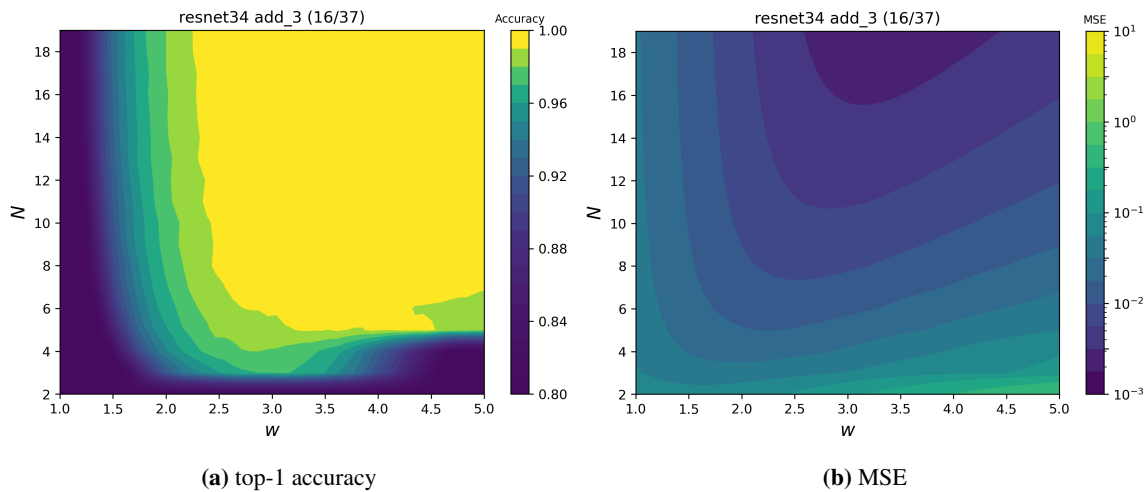


Figure 2.5: Analysis of “per-neuron distribution” uniform quantization scheme with N quantization levels and clipping range $[\mu_i - w\sigma_i, \mu_i + w\sigma_i]$, where w is the clipping width (in units of σ_i), and μ_i and σ_i are respectively the mean and standard deviation of the neuron output distribution Y_i . (a) Plot of inference accuracy of the reconstructed tensor resulting from quantization and dequantization of intermediate tensor. Accuracy is scaled relative to baseline accuracy computed from regular model inference on the given dataset. The darkest color represents $\leq 80\%$ accuracy. (b) Plot of MSE between the original tensor and the reconstructed tensor.

2.2 Reusing image codecs

There has been much work already done in image compression. We can use this to our advantage and attempt to repurpose image codecs to work with tensor data. For this to occur, some additional work (e.g. tiling) needs to be done to convert the tensor into the correct format for codec input.

2.2.1 Tiling

To allow a 3-d HWC tensor² to be inputted into an image codec, it must be reduced to a 2-d tensor, while preserving useful structure (e.g. spatial locality) where possible. Consider the feature map of the intermediate tensor of a CNN in Figure 2.6. The intermediate tensors of CNNs tend to contain many spatial redundancies *within* channels (and indeed, *across* channels as well). We note these redundancies in the following equations:

$$T(y, x, c) \approx T(y + \Delta y, x + \Delta x, c) \quad (\text{intra-channel}) \quad (2.5)$$

$$S(c, c') \geq d\left(\frac{1}{\sigma_c}[T(c) - \mu_c], \frac{1}{\sigma_{c'}}[T(c') - \mu_{c'}]\right) \quad (\text{inter-channel}) \quad (2.6)$$

where T is a 3-d HWC tensor and $S : \{1, \dots, C\} \times \{1, \dots, C\} \rightarrow \mathbb{R}$ represents some bound on the distance d between a pair of channels. Note that a conventional distance metric on vector spaces, such as an ℓ_2 -norm, is not necessarily the best choice: the convolutional kernels from the last convolutional layer may offset pixels, or invert the feature map. It is perhaps better to apply the conventional distance measure on the normalized channels after they have been “blurred” by a max-pool with the stride length equal to the width of the convolution kernels. That is, $d'(T_c, T_{c'}) = \|\text{maxpool}(T_c) - \text{maxpool}(T_{c'})\|_2$. Then, to account for channels with “negative” edge polarity (i.e. background darker than the edges), one could set $d(T_c, T_{c'}) = \min(d'(T_c, T_{c'}), d'(T_c, -T_{c'}))$.

A tiling strategy that keeps nearby channels together involves simply assigning each channel to a $C_W \times C_H$ grid, where each grid entry is of size $W \times H$. The result should be a 2D image of size $(C_W \cdot W) \times (C_H \cdot H)$. To ensure there are enough available grid entries for all the channels, $C \leq C_W \cdot C_H$. One should also keep in mind that some image codecs require or prefer that the image dimensions be reasonably similar.

Because the image will be storing a quantized tensor, it is preferable that the color information be stored with an indexed color palette. However, not all codecs support indexed or 8-bit color. For such codecs, the tensor value may be stored in RGB or YUV color models. One should note that some codecs will convert RGB to YUV prior to encoding (and back to RGB when decoding). This is done because luminance (Y) and chroma (UV) can be encoded separately at different rates; a common format is 4:2:0, which stores twice as many luminance pixels as chroma pixels. If the entirety of the RGB color model is used, the conversions to and from YUV can be destructive. Thus,

²The indices of a HWC tensor are along the dimensions of height, width, and channels.

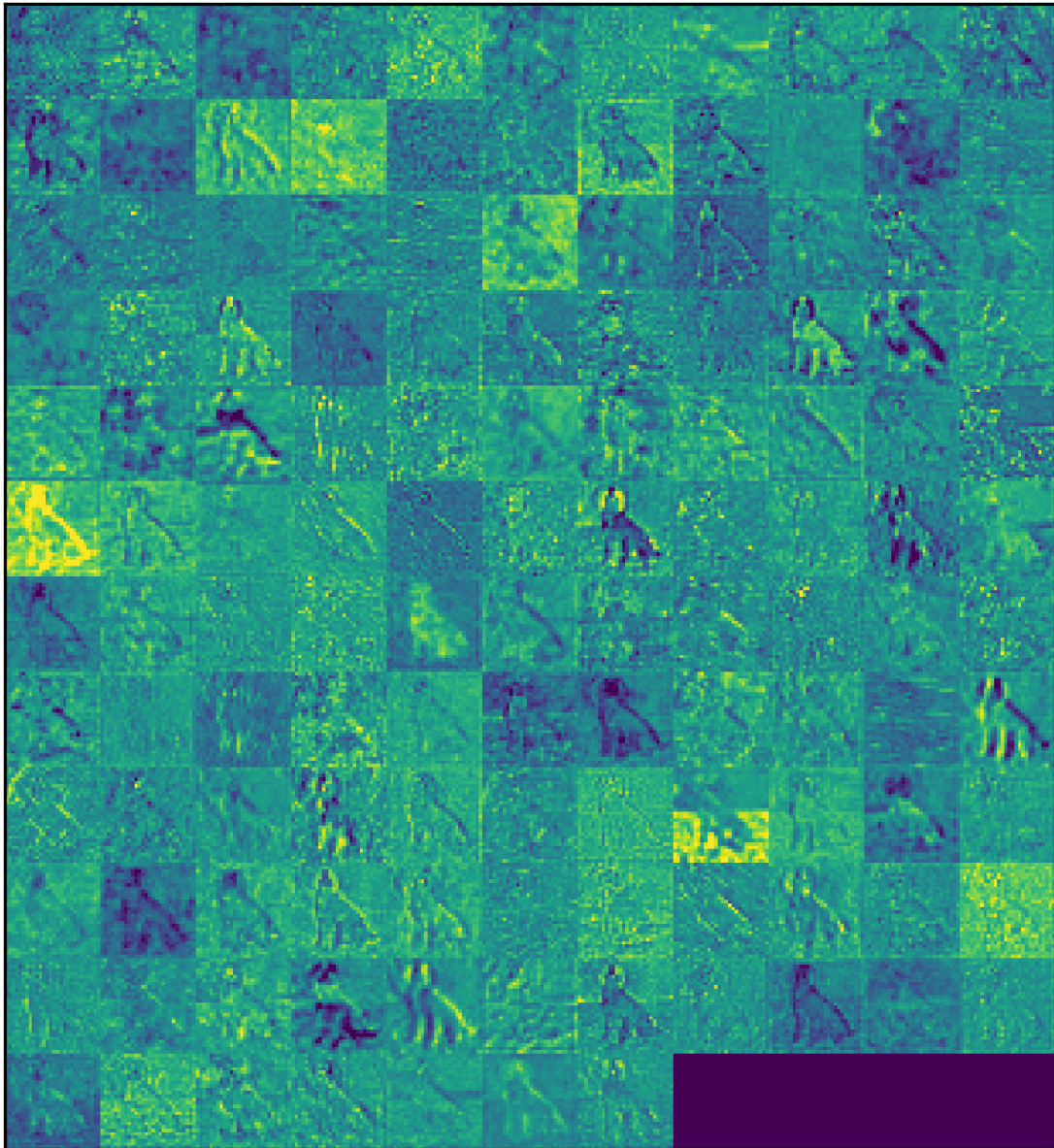


Figure 2.6: Feature map of add_3 layer of ResNet-34 on input image of dog. Intra-channel redundancy exists in the form of similarities in intensity between nearby pixels. Inter-channel redundancies manifest themselves across clusters of channels. For instance, some channels have sharp edges outlining the dog; others and others contain few distinguishable edges. The similarities across channels are more apparent after normalizing the channels with respect to their mean μ_c and variance σ_c . However, these edges are not distinguishable in the feature maps of tensors quantized to a low level count, as in Figure 2.3. Nonetheless, such quantization only experiences $< 0.5\%$ drop in accuracy, suggesting that the visual fidelity of the edges is not very important for performing accurate inference.

when using RGB with such codecs, it is best to represent a single tensor element as an RGB pixel with the R, G, and B components sharing the same intensity value. When storing in YUV directly, image codecs such as JPEG do not differentiate between compression techniques and parameters used for Y and UV data, so it is acceptable to store a tensor element in *either* a Y, U, or V component. In the case of JPEG, the Y, U, and V planes are compressed separately; macroblocks only consist of one color component at a time. Some JPEG encoders and decoders also support grayscale images which consist of only the Y component.

2.2.2 JPEG

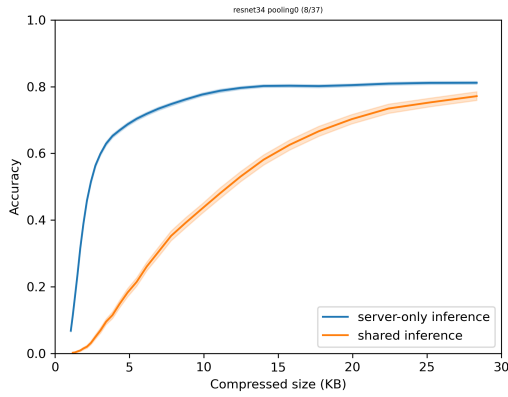
Though JPEG is a fairly old standard for image compression and many newer codecs and technologies have been developed since its introduction in 1992, it is still widely used, and it is a good starting point to consider given its ubiquity. JPEG first transforms the input image by applying a discrete cosine transform (DCT) to macroblocks (8×8 or 16×16) to exploit spatial redundancies, and then scaling by a cleverly weighted quantization table³ which allocates a larger number of bits to low frequency coefficients. The resulting coefficients are then run-length encoded (RLE) and entropy coded via Huffman coding.

By tiling the tensor in the manner described in Section 2.2.1, we are able to keep channel data contained within as few macroblocks as possible and maintain contiguity across the height and width tensor dimensions. This helps the DCT exploit spatial intra-channel redundancies. Unfortunately, this comes at the cost of exploiting inter-channel redundancies: the DCT is local to each macroblock, and thus cannot look across channels.

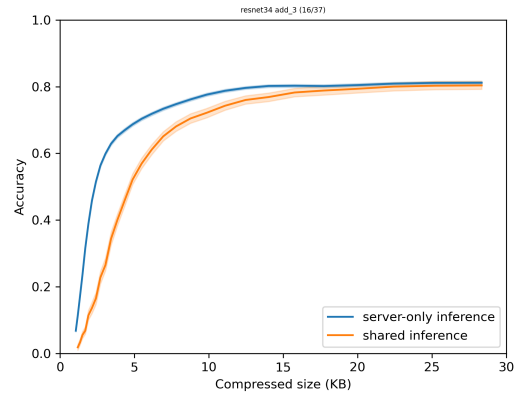
Images and video, the primary types of input data for CNNs, already possess expert-designed compression codecs. Thus, in order to be competitive with a server-only inference strategy (Figure 1.1b), one needs to compare the compressibility of input data with intermediate tensor data. Since JPEG is lossy, in Figure 2.7 we compare the model accuracy performance of applying JPEG compression to input data versus applying it to tensor data at various output file sizes.

The methodology for generating these plots is described as follows. The input image dataset is generated by taking image samples from ImageNet (1000 classes), cropping them to a ratio of 1:1, downscaling to 224×224 , saving the resulting images again as JPEG images, and filtering out images that are not within a file size of 30 ± 0.3 KB. From these, we keep a sample set of 4096 images (with 4–100 images representing each class), and then compress them via JPEG at a variety of quality levels for each image, generating over 100,000 compressed JPEG images at varying file sizes. The resulting JPEG images are binned into logarithmically spaced intervals within the range 1 KB – 30 KB, taking care that no bin contains more than one JPEG generated from the same source

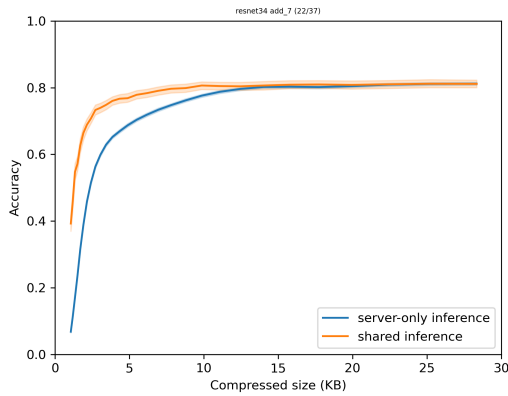
³Typically, the quantization table is precomputed. Most JPEG encoders such as libjpeg [16] use the IJG standard quantization tables [17]. Another popular set of quantization tables are the proprietary Adobe Photoshop quantization tables. On the other hand, some encoders (typically those that are built into cameras) use adaptive quantization tables that are generated on-the-fly based on the image being compressed. [18], [19]



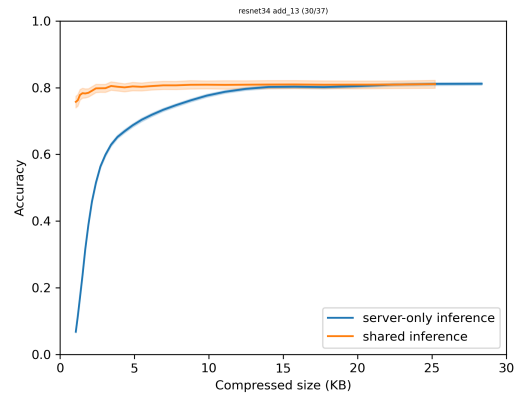
(a) ResNet-34, pooling₀ layer, $56 \times 56 \times 64$



(b) ResNet-34, add₃ layer, $28 \times 28 \times 128$



(c) ResNet-34, add₇ layer, $14 \times 14 \times 256$



(d) ResNet-34, add₁₃ layer, $7 \times 7 \times 512$

Figure 2.7: Top-1 image classification accuracy vs JPEG compressed frame output size across various layers of ResNet-34. For shared inference, tensor data was stored in the Y (luma) component in tiles. Pre-trained model [20] trained on ImageNet (1000 classes). Tested on ImageNet. Results for more layers can be found in Appendix A.

image. Inference is then performed on these binned images, and the top-1 accuracy is computed for each bin. The result is plotted as the *server-only inference* curve.

The sample set of 4096 source images is then taken again, but this time the images are run through the client-side model. The resulting tensors are then quantized to 256 levels (8 bits) and tiled. Then, they are inserted into the luminance channel and JPEG compression is applied to them at a variety of quality levels, resulting in over 100,000 compressed tensors. The resulting compressed tensor data is then binned using the same process as for the server-only inference, ensuring that no bin contains more than one compressed tensor generated from the same source image. These bins are then run through server-side model inference and the resulting top-1 accuracies are plotted in the *shared inference* curve.

As expected, the model accuracy falls due to reconstruction errors as the compressed output size shrinks. The point at which the accuracy falls below a particular threshold varies depending on the split point. In general, the accuracy curves tend to rise as we split at deeper layers in the model. Note that the accuracy curves may still fall at deeper layers due to a variety of reasons such as larger tensor dimensionality, changes in neuron output distribution, and reduced resilience to reconstruction errors.

Because JPEG compression codecs such as libjpeg [16] and libjpeg-turbo [21] offer no bitrate controls, it is tricky to control the size of the output. The primary control for rate/distortion offered by JPEG encoders is the **quality factor**, which ranges between 1-100 and typically controls the DCT coefficient quantization table. Because of the entropy coding which follows the quantization process, it is difficult to predict the output size. This creates some difficulty in maintaining a constant bitrate to adhere to network bandwidth and quality constraints and also in maintaining a stable model accuracy. Indeed, if one is not careful, the bitrate can fall into a range where inference accuracy is poor.

2.2.3 JPEG 2000

We now consider JPEG 2000 [22], the successor to the JPEG format. In contrast to JPEG's block-based DCT, JPEG 2000 uses a discrete wavelet transform (DWT) which can be applied to the image globally. Thus, JPEG 2000 avoids blocking artifacts and also exploits larger redundancies across the image. Similar to JPEG, the resulting transform coefficients are quantized and entropy coded, though with more sophisticated techniques. These techniques also enable fine-grained bitrate control via rate-distortion optimization. This makes JPEG 2000 a more predictable codec than JPEG.

Figure 2.8 plots the model accuracy versus output size. These are generated in a similar way to the JPEG curves in Figure 2.7; however, instead of trying all possible values of an arbitrary control like quality level, JPEG 2000's bitrate controls are used to precisely specify the desired output sizes. This is much quicker (less samples need to be tried to find a matching output sizes), leads to a more uniform distribution of samples, and reduces the variance in the dependent variable (output size).

Surprisingly, for server-only inference, the resulting accuracy at low bitrates is consistently worse than JPEG. This is somewhat unexpected, since JPEG 2000 should perform better than JPEG at

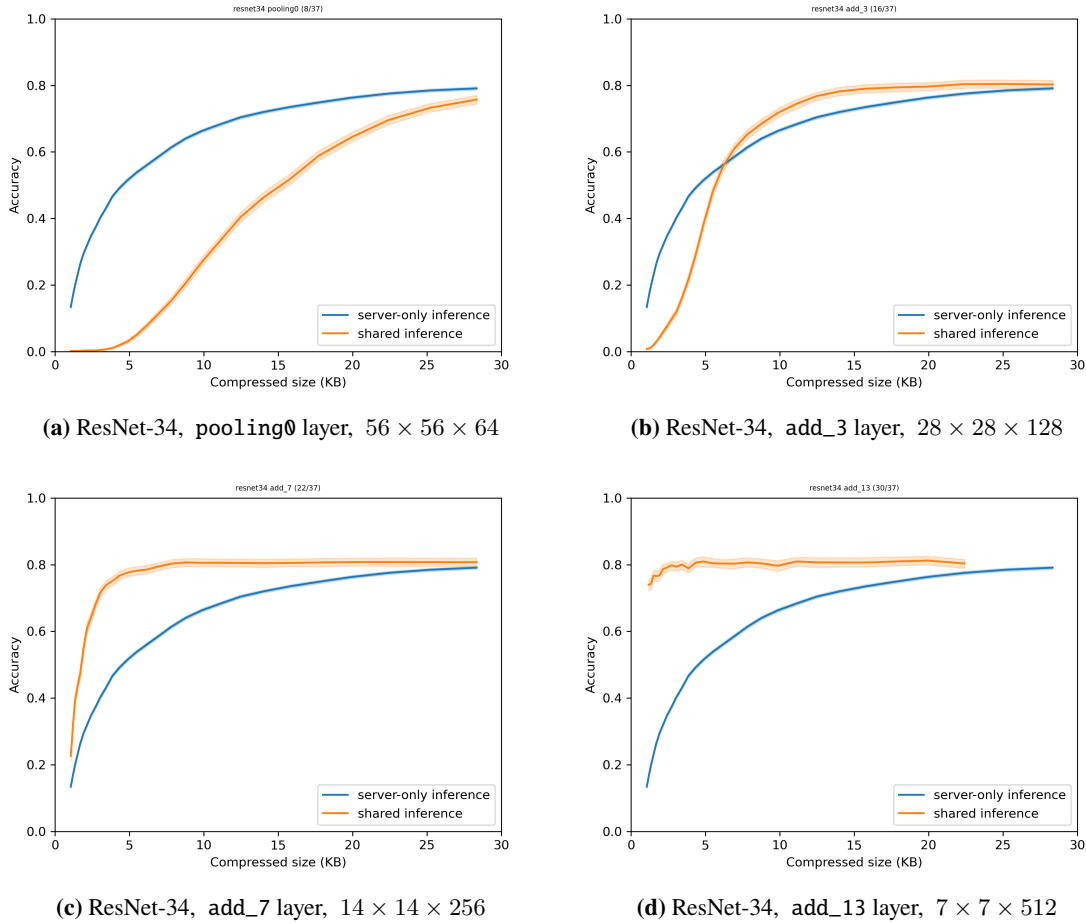


Figure 2.8: Top-1 image classification accuracy vs JPEG 2000 compressed frame output size across various layers of ResNet-34. Results for more layers can be found in Appendix A.

low bitrates. This occurs possibly because ImageNet images are already in the JPEG format and re-encoding JPEGs to JPEGs while only changing the quality level parameter merely corresponds to a rescaling of the quantization table; whereas transcoding from JPEG images to JPEG 2000 images requires a more significant change in the compression technology (from DCT to DWT) and must also deal with the JPEG artifacts present in the source image. Another possible explanation is that the JPEG 2000 encoder being used (OpenJPEG [23]) is not optimized for such low bitrates.

On the other hand, the shared inference curves sometimes provide useful characteristics. For instance, to maintain an above 99% accuracy in the add_7 layer of ResNet-34, JPEG requires at least 9 KB tiled tensor, whereas JPEG 2000 only requires 7 KB per tiled tensor. As bitrates get even lower, JPEG once again begins to outperform JPEG 2000.

2.3 Summary

In this chapter, we saw that models containing BatchNorm layers provide good candidate layers to split upon. The aggregate output distributions of BatchNorm layers and the layers that follow BatchNorm layers often approximate normal distributions or other light-tailed distributions. Furthermore, the individual neuron outputs of these layers can be treated as light-tailed distributions over a large number of input samples. We also saw that the means of neuron outputs, computed over a large number of samples, were reasonably uniform across a given channel. Their standard deviations also showed spatial uniformity in the x and y directions for a fixed channel.

Next, we looked at how applying uniform quantization with various intervals and levels affected final inference accuracy. For the ResNet-34 model at the `add_3` layer, we saw a drop in top-1 accuracy by $< 0.5\%$ when quantizing to 7 levels (2.8 bits/tensor element). Normalizing the tensor by the by computed means and standard deviations for each individual neuron output before quantizing allowed us to reduce the level count to 6 levels (2.6 bits/tensor element) in order to achieve the same top-1 accuracy.

Next, we looked at how to bring existing image codecs to work with tensor data. To allow this, we first reshaped the 3-d tensor data into a 2-d format. Because image codecs rely upon spatial redundancies within an image to compress the image, it is important to reshape in such a way that tensor elements with similar intensity values are kept close together. For CNNs, we noted two primary redundancies: intra-channel and inter-channel. To exploit the intra-channel redundancies, we tiled the channels into a 2-d grid. Next, we quantized the reshaped data to 8-bit integers and then fed it into the JPEG and JPEG 2000 codecs. Increasing the amount of image compression we applied to each tensor reduced the top-1 accuracies. We discovered that as we progress through the model's layers, the top-1 accuracy for a given compression ratio *usually* increases. This is due to reduced dimensionality of the tensor, changes in the neuron output distributions, and increased resilience to reconstruction errors. At a certain layer, shared inference accuracy becomes larger than server-only inference accuracy for some size of compressed data. For ResNet-34 with JPEG compression, shared inference consistently met or outperformed server-only inference across all compression sizes at the `add_7` layer, which takes roughly a third of the total computational expense of the model to compute.

As we will see in Section 4.2, this provides promising results, and demonstrates how shared inference may situationally outperform server-only inference for some combinations of hardware and network conditions. With better compression methods that can exploit the inter-channel redundancies in addition to the intra-channel redundancies we made use of here, it is likely that shared inference can outperform server-only inference at perhaps even earlier layers, further improving the usefulness of the shared inference strategy.

Chapter 3

Towards tensor streams

In the previous chapter, we looked at how to compress single tensors for transmission and inference. But often, one is concerned with the inference of a *sequence* of inputs. For video, there is typically a strong relationship between successive input frames. In this chapter, we will show that the sequence of intermediate tensors generated from the input sequence also share temporal similarities. Furthermore, during transmission of a real-time tensor stream, some tensor data may be lost or corrupted; we will also discuss how to continue with inference despite the loss of this information.

3.1 Input transformations

In order to develop techniques for encoding a stream of tensors, we should use typical transformations of the input to determine what changes in the intermediate tensor are typical.

For video, common transformations that occur within the input frame include translation (panning/tilting), rotation, and rescaling (zoom) of groups of pixels. As such, one of the key ideas used by video codecs is the idea of motion compensation [24]. This involves estimating the motion vectors for the current frame with respect to a reference frame. A prediction of the current frame is reconstructed by mapping the motion vectors over the reference frame. The difference is then computed between the current frame and the predicted frame; typically, this difference is small in magnitude. Along with the motion vectors, the difference is then encoded and stored. Due to the temporal redundancies in a sequence of frames, this can often result in significant savings in comparison to encoding the current frame without motion compensation.

Here, we consider global translation of frames. For simplicity, we will only consider inputs which are translated horizontally and equally for every pixel. In Figure 3.1, we translate the reference frame by amounts that are integer multiples $k\frac{w_I}{w}$ of the image width w_I divided by the tensor width w . In a CNN such as ResNet-34, this induces, roughly, a translation of the tensor T in the x direction by k pixels. This is due to the translation invariance, which comes from the fact that all preceding layers are convolutional, pooling, batch normalization, ReLU, or addition layers from the skip connections.

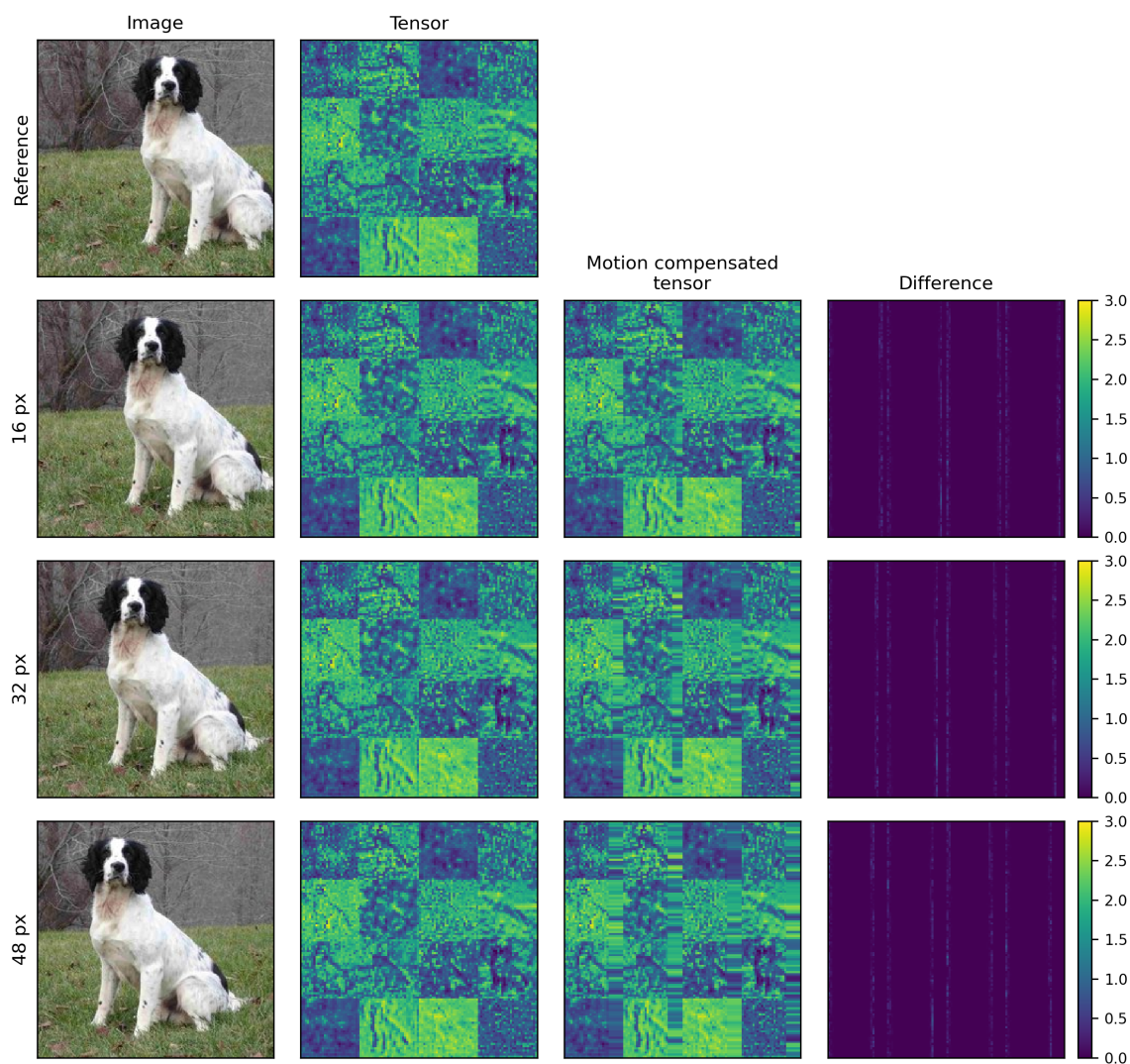


Figure 3.1: The input image ($224 \times 224 \times 3$) is horizontally translated by 16px, 32px, and 48px with respect to the initial reference frame (top). This corresponds to estimated horizontal translations in the intermediate tensor of the `add_3` layer of ResNet-34 ($28 \times 28 \times 128$) by 2px, 4px, and 6px, respectively. The second column shows a select portion of the feature map of the intermediate tensor corresponding to each translated image. The third column shows the feature map of a tensor predicted by applying motion compensation on the reference tensor. The fourth column shows the absolute difference between the ground truth and the prediction, where the boundary regions that cannot be motion compensated have been zeroed. The PSNR of the non-boundary regions ranges between 90–92 dB. Interestingly, the difference in the interior regions of each channel is exactly 0. This occurs due to a combination of the translation invariance of preceding convolutional layers and strides of preceding pooling layers. Note that the colormaps have been adjusted for visual clarity.

We can form a reconstruction \hat{T} of the original tensor by:

$$\hat{T}(y, x, c) = T_{\text{ref}}(y + v_y(x, y), x + v_x(x, y), c) \quad (3.1)$$

where $v : \mathbb{R}^2 \rightarrow \mathbb{R}^2$ is computed through motion estimation of the current input frame with respect to reference input frame, and rescaling the resulting vectors by $\frac{w_l}{w}$. To assess the correctness of the reconstruction, we define the peak signal-to-noise ratio (PSNR) for a tensor T and its reconstructed tensor \hat{T} by:

$$\text{MSE} = \|\hat{T} - T\|_2^2 = \frac{1}{HWC} \sum_{x=1}^W \sum_{y=1}^H \sum_{c=1}^C (\hat{T}(y, x, c) - T(y, x, c))^2 \quad (3.2)$$

$$R = \max T - \min T \quad (3.3)$$

$$\text{PSNR} = 10 \log \frac{R^2}{\text{MSE}} \quad (3.4)$$

However, since not every pixel has a valid motion vector w.r.t. the reference frame, we will ignore those regions in our calculations, for this synthesized example. For these translated frames, the PSNR for the valid regions is computed to be 90–92 dB. In fact, the interior regions of the reconstructed tensor are *exactly* equal to the original tensor. This is likely due to the alignment of the pooling layers.

To get a more realistic picture for the effect of global translations in reconstruction, we let k be non-integer so that the motion estimated vectors for the tensor are also non-integer. Figure 3.2 shows an example of this. Unsurprisingly, the reconstruction error has increased, resulting in a PSNR of 74–75 dB.

Motivated by these observations, one can imagine the following compression strategy: precompute the motion compensation vectors on a scaled version of the input frame. (This should be easier to do on the input frame rather than a given channel since the input is less noisy.) Then, reuse the computed motion vectors across all channels. Such an approach is both more computationally efficient and potentially allows for better compression since different sets of motion vectors do not have to be stored for each channel individually.

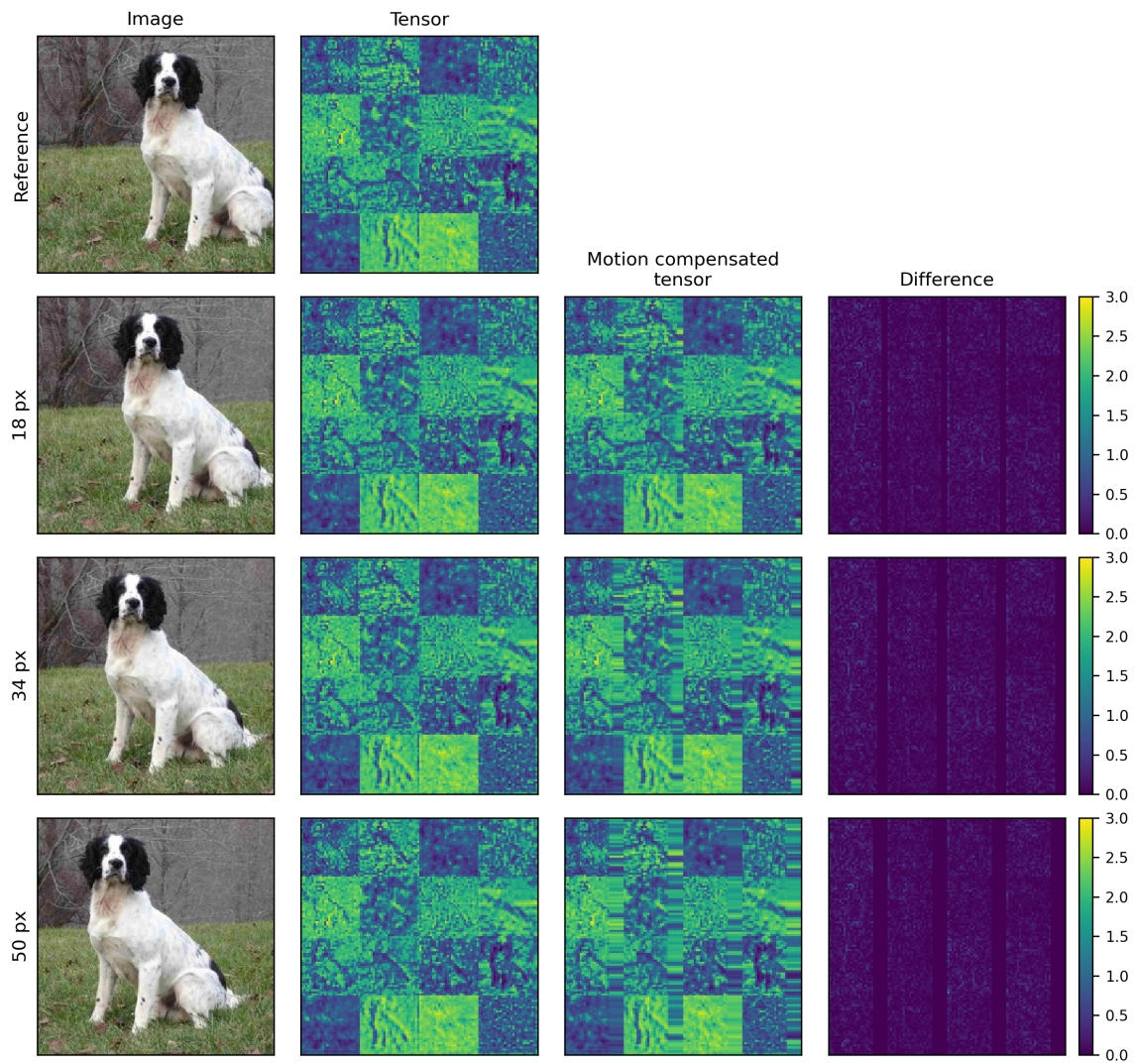


Figure 3.2: The input image ($224 \times 224 \times 3$) is horizontally translated by 18px, 34px, and 50px with respect to the initial reference frame (top). This corresponds to estimated horizontal translations in the intermediate tensor of the `add_3` layer of ResNet-34 ($28 \times 28 \times 128$) by 2.25px, 4.25px, and 6.25px, respectively. The second column shows a select portion of the feature map of the intermediate tensor corresponding to each translated image. The third column shows the feature map of a tensor predicted by applying motion compensation on the reference tensor. The fourth column shows the absolute difference between the ground truth and the prediction, where the boundary regions that cannot be motion compensated have been zeroed. The PSNR of the non-boundary regions ranges between 74–75 dB. Note that the colormaps have been adjusted for visual clarity.

3.2 Error concealment

In the event that some tensor data is corrupted or lost during transmission, we should still attempt to give the best inference possible with the data that remains. In this section, we investigate common forms of data loss and seek to determine a tensor reconstruction strategy in the event of data loss. More advanced strategies for recovering data utilize tensor completion methods [25], but we will not be considering those here. It should be emphasized that the primary objective here is not to minimize reconstruction error; rather, it is to obtain the best inference accuracy.

Figure 3.3a summarizes the performance of various data recovery strategies for the data loss of random tensor elements from a particular layer of ResNet-34, and Figure 3.3b summarizes analogous results for the data loss of entire tensor channels. Each data point is computed over 16,384 samples representing 1000 classes¹ from the ILSVRC 2012 dataset. The various strategies are described in order below.

The simplest strategy for dealing with missing tensor data is to fill that portion of the tensor with the value 0. As expected, this is the poorest strategy and produces a curve that drops fairly quickly in terms of inference accuracy (and would likely perform even worse for layers that do not generate tensor data with near-zero mean).

A second strategy is to set the missing tensor data to the mean of its channel. This requires the client to compute the channel-by-channel means and transmit these means alongside the remaining tensor data. When $C \ll HWC$, the amount of additional bandwidth taken by these means is minimal, though prediction, quantization, and entropy coding techniques can likely be applied to them as well if needed.

A third strategy that fares better is to set the missing tensor data to the statistical mean of tensor values derived over some set of known data samples. In this case, the samples are taken from partial inferences of ImageNet (1000 classes); in fact, a feature map of this particular statistical mean of tensor values was shown earlier in Figure 2.4a. The performance of this strategy should improve further if the mean is taken over a more representative sample set — for instance, sample tensors generated from the previous frames of a video, the audio background noise, or the previous audio chunks of an audio stream. In contrast to the second strategy, this does not require any additional data transmission.

A fourth strategy involves taking a hybrid approach to previous two strategies: the reconstructed missing tensor element \hat{T} is defined by $\hat{T}(y, x, c) = \mu(y, x, c) + \left(T_\mu(c) - \frac{1}{HW} \sum_{i,j} \mu(i, j, c)\right)$, where μ is the mean of tensors over a representative sample set, and T_μ is the transmitted channel-by-channel mean.

These strategies perform roughly the same regardless of whether it is random tensor elements or entire channels that are missing. Overall, filling in missing tensor elements with their expected value precomputed over the dataset seems to perform better than setting it to the channel’s actual mean

¹Each class is represented by 4–100 samples.

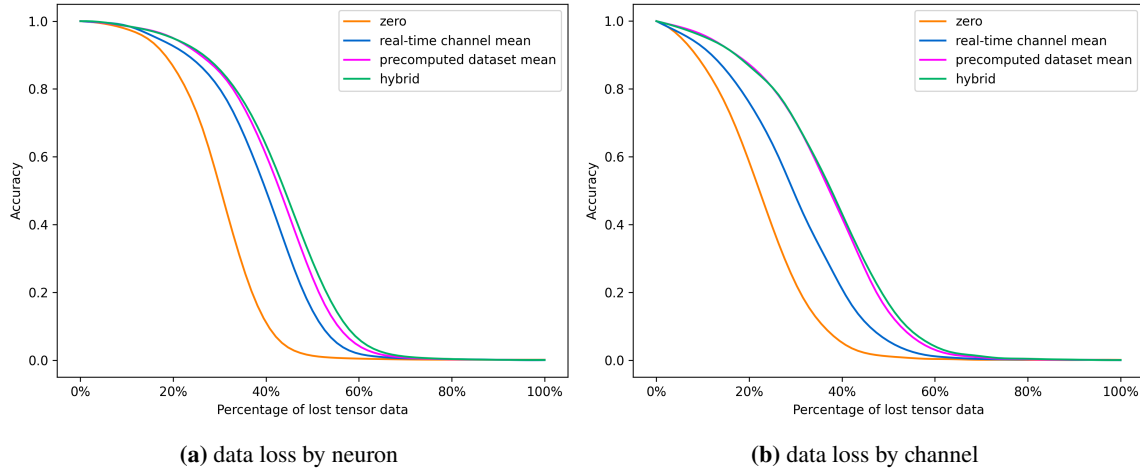


Figure 3.3: Accuracy versus amount of data loss, with application of various data recovery strategies on `add_3` layer of ResNet-34.

computed at runtime. The hybrid approach of these does not perform any better at low proportions of missing tensor data, and only marginally performs better at higher proportions.

These methods do not make use of the various spatial and temporal redundancies that occur within a tensor stream. Regardless, they perform well enough for low proportions of missing tensor data: if 5% of the tensor is missing, there is only a 0.2% drop in accuracy; for 10% missing, a 2% drop in accuracy; and for 20% missing, a 5% drop. If the drop in accuracy meets an acceptable threshold, these methods can provide a simple and computationally inexpensive way of recovering the tensor. If a sufficiently large portion of the tensor is lost, one can then swap to more sophisticated methods of tensor recovery, in order to maintain an accuracy threshold.

3.3 Summary

In this chapter, we looked at some useful properties within the tensor stream that can be exploited for better tensor stream compression. For CNNs acting on video input, successive tensors within the stream respond in the same way as successive video frames do to common transformations (e.g. translations) within the image. Furthermore, errors in a tensor stream can be partly concealed by reasonably simple methods such as filling in missing tensor elements with the mean value. This is because the end goal is the accuracy of inference rather than merely reducing reconstruction error. Simple error concealment methods such as these are also useful because of their predictability and lower computational resource load in comparison to more advanced techniques.

Chapter 4

Implementation

Though the primary challenge for collaborative intelligence is compression, there are also other challenges that occur in practice. Such challenges include the work needed to develop a full inference pipeline across various edge devices, choosing the best inference strategy depending on hardware and network conditions, minimizing inference latency through the use of custom network protocols, and improving ease of use for software developers that wish to use collaborative intelligence in their own applications.

This chapter looks at how to bring collaborative intelligence out of the research lab and into the real world. First, we will discuss a proof-of-concept implementation that was developed for Android, and an inference pipeline that allows interchangeability between its various components. Next, we will describe how total inference latency varies depending on the model, strategy, hardware performance, and network conditions. Then, we will propose a blueprint for a network protocol customized for transmitting real-time tensor streams, keeping in mind latency, throughput, and backpressure. Lastly, we will look at some library code that was developed to help conduct research and also functioned as part of the proof-of-concept.

4.1 Prototype

A complete prototype was designed to demonstrate and help compare between server-only, client-only, and shared inference strategies for a variety of models. To function as the mobile edge client, an Android app¹ was written in Kotlin and RenderScript, utilizing the TensorFlow Lite, Fotoapparat, and RxJava libraries. A screenshot of the app in action is shown in Figure 4.1. To perform the server-side inference, a server² was written in Python to receive and process inference requests. Finally, a GUI app for desktop or web clients³ was written in TypeScript, NodeJS, and the Electron

¹<https://github.com/YodaEmbedding/collaborative-intelligence/tree/thesis/android>

²<https://github.com/YodaEmbedding/collaborative-intelligence/blob/thesis/server.py>

³<https://github.com/YodaEmbedding/collaborative-intelligence/tree/thesis/server-monitor>

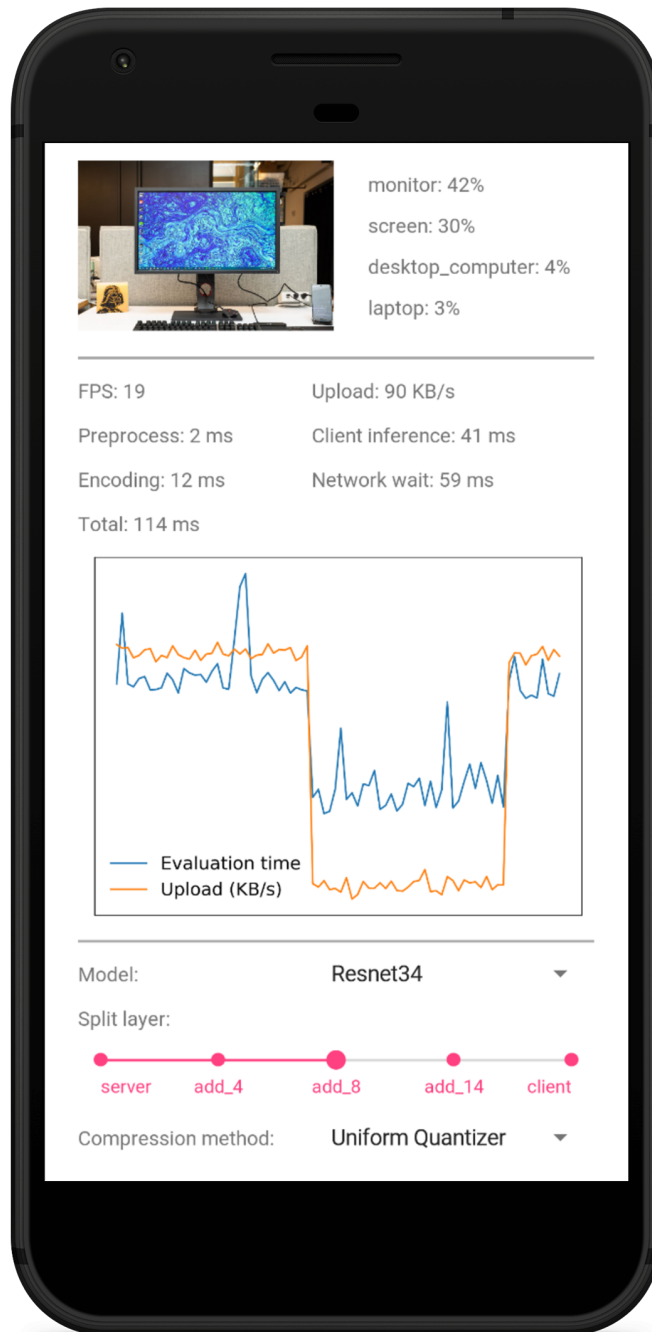


Figure 4.1: Demo app running on Android device. One may choose between the model, layer split points, feature tensor compression method, and also control the available upload bandwidth. Plots total inference time and serialized/compressed tensor upload size for each frame.



Figure 4.2: Live demo of prototype at NeurIPS 2019.

framework to display a preview of the server’s reconstructed tensor, debugging information, and any other additional real-time statistics. The models available include various ResNet models (18, 34, 50, 101, 152) and VGG, though one can add additional models by splitting the model, converting it to `.tflite` format, and adding the relevant entries to `models.json` (see repository for details).

4.1.1 NeurIPS demo

The prototype was demonstrated live at the NeurIPS 2019 conference. A paper describing the demo is available in [11]. Two Android devices were used as clients; one client was connected to a nearby server on a LAN, and the other client was connected to a remote server in a nearby city. Each server utilized an NVIDIA GeForce GTX Titan X GPU, whereas the clients utilized the Qualcomm Snapdragon 845 and Qualcomm Snapdragon 855 SoCs. Figure 4.2 contains a photo of the interactive demo booth from this event.

4.1.2 Inference pipeline

Figure 4.3 shows a flowchart overview of the complete inference pipeline. The pipeline takes an input signal, preprocesses it, runs it through the client-side inference model, applies encoding on

partially inferred tensor (on the GPU), serializes the resulting tensor via a *postencoder* (which runs on the CPU or other dedicated hardware), transmits the data over the network, deserializes with a corresponding *predecoder*, applies decoding on the deserialized tensor (on the GPU), runs the reconstructed tensor through the server-side inference model, and finally sends the result of the complete inference back to the client.

The client begins by notifying the server which model to use. When the client needs to initialize or change the model and other configuration settings, a `ModelSwitchRequest` is made. This sends over details including the model, split layer, encoder, and postencoder. Once the inference pipeline is configured and ready, the server replies with a `ModelReadyResponse`. This ensures that the model and postencoder are preloaded and that the perceived server inference latency is minimized for when the client sends its first inference request to the server.

Frames that are inputted into the pipeline often require preprocessing. `RenderScript` is used to preprocess the input frames efficiently. The camera input is converted from YUV to RGB, cropped to 1:1, resized to 224×224 , rotated to an upright orientation, and converted to float, before being fed into the client-side model. The reshaping/tiling code could also be converted to `RenderScript` for better performance, though the current Kotlin-only implementation is quick enough for small tensor sizes.

The encoder is attached to the end of the client-side model, and is a part of the deep model itself. The encoder can be a trainable network, such as the reduction unit of a “butterfly unit” [26], which reduces the size of the tensor. Or it can simply be a quantizer, handling data-heavy computations directly with a GPU, before the data is transferred to RAM. For instance, the `UniformQuantizationU8Encoder` layer uniformly quantizes the floating-point values of the preceding layer to an 8-bit `uchar` over a fixed clipping range.

After the encoder runs, the tensor output is copied from GPU memory to RAM. From here, it is fed into the postencoder, which runs on the CPU or a dedicated hardware chip (e.g. H.264 ASIC). The postencoder is a codec such as JPEG, PNG, H.264, or some other custom codec. The postencoder handles any necessary reshaping and tiling of the tensor, and outputs a compressed byte stream that can be transmitted over the network; in the current implementation, this is done over TCP. Analogous to the client-side postencoder, there is a server-side predecoder, which decodes the byte stream, and feeds the resulting tensor into the server-side model. Attached to the beginning of the server-side model is a decoder corresponding to the encoder at the end of the client-side model. This decoder reconstructs the tensor to be of the correct data type and shape, before propagating the tensor through the rest of the model.

The prediction tensor outputted from the server-side inference can be sent back to the client, optionally after a further processing/decoding step. In the case of the demo app and server, the probability vector is decoded into the top-n labels and probabilities. Along with the request id and measured server-side inference latency (useful for rate limiting and monitoring statistics), these are sent back in a `ResultResponse`. An example JSON serialization of this is given:

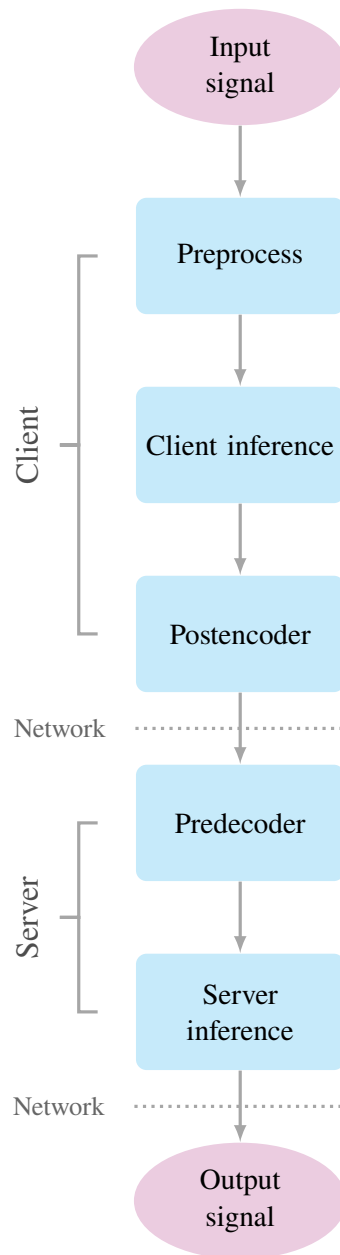


Figure 4.3: Full inference pipeline. An input signal is preprocessed (e.g. an image is cropped, resized, and normalized). Then, it goes through the first half of the inference model on the client. The intermediate tensor is also passed through a simple GPU-based encoder (e.g. an 8-bit quantizer) attached to the end of the client-side model. This tensor is then more heavily compressed by the *postencoder*, which may perform its operations on the CPU or on a dedicated hardware chip for codecs. This outputs a serialized stream of bytes that can be transmitted over the network. The server receives the byte stream and feeds it into the *predecoder*, which deserializes the byte stream into a tensor. This tensor is then inputted into the server inference model, which is prefixed by a decoder that reconstructs an approximation of the original tensor. Finally, the resulting output signal is serialized into a byte stream and transmitted back to the client.

```

{
  "frameNumber": "<int>",
  "inferenceTime": "<int>",
  "predictions": {
    "label": {"name": "<str>", "description": "<str>", "score": "<int>"},
    "label": {"name": "<str>", "description": "<str>", "score": "<int>"},
    ...
  }
}

```

To prevent overloading the network with too many write requests, no new inference requests are made by the client until a `ConfirmationResponse` (containing a unique frame request id and the number of bytes received) is received from the server.

4.2 Latency model

The total inference latency for a shared inference strategy can be expressed as a sum of various parameters:

$$I_t = \underbrace{I_c + E_c}_{\text{client-side}} + \underbrace{\frac{D}{B}}_{\text{network}} + \text{RTT} + \underbrace{E_s + I_s}_{\text{server-side}} + \epsilon \quad (4.1)$$

where

- I_t = total inference time
- I_c = inference time of client-side model
- I_s = inference time of server-side model
- E_c = serialization/encoding time for client output tensor
- E_s = deserialization/decoding time for server input tensor
- D = size of serialized/compressed tensor data
- B = rate of data transfer (bandwidth)
- RTT = round trip time
- ϵ = other latencies (negligible)

The values of these parameters vary wildly depending on the hardware, network conditions, the model, choice of split layer, and available compression options. A particular strategy $\Omega^{(l)}$ can be associated with a 4-tuple $(I_c^{(l)}, E_c^{(l)}, E_s^{(l)}, I_s^{(l)})$. Then we may write the total inference latencies

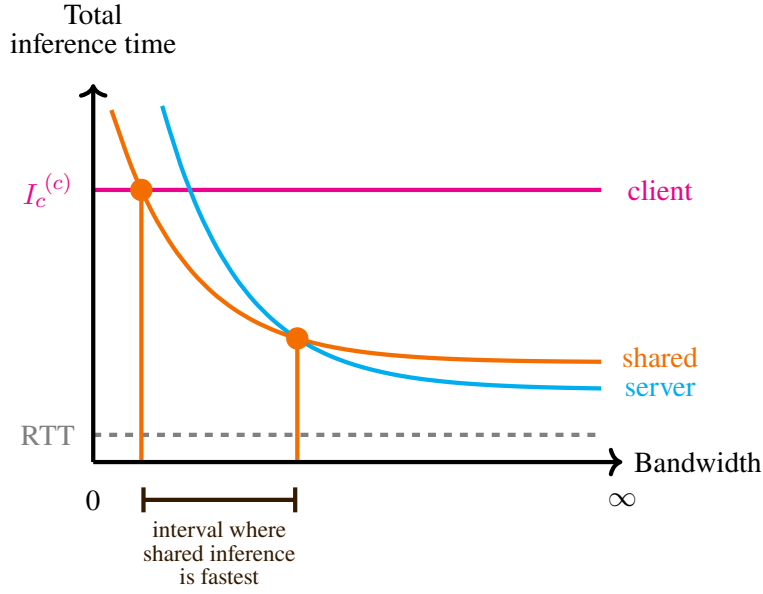


Figure 4.4: Total inference latency versus bandwidth for the given conditions (4.6). Lower is better. At zero bandwidth, client-only inference performs best. However, shared inference becomes dominant as bandwidth increases, until finally, server-only inference surpasses shared inference due to faster server-side hardware and the benefits of transmitting less data becoming less significant.

for the various strategies as:

$$I_t^{(l)} = I_c^{(l)} + E_c^{(l)} + E_s^{(l)} + I_s^{(l)} + \text{RTT} + \frac{D^{(l)}}{B} = b^{(l)} + \frac{D^{(l)}}{B} \quad \text{split layer } l \quad (4.2)$$

$$I_t^{(s)} = E_c^{(s)} + E_s^{(s)} + I_s^{(s)} + \text{RTT} + \frac{D^{(s)}}{B} = b^{(s)} + \frac{D^{(s)}}{B} \quad \text{server-only} \quad (4.3)$$

$$I_t^{(c)} = I_c^{(c)} = b^{(c)} \quad \text{client-only} \quad (4.4)$$

To compare a particular shared inference strategy with a client-only or server-only inference strategy, or even other shared inference strategies, we can fix the round trip time (RTT) across strategies and vary bandwidth (B). Then, if the following conditions

$$0 = D^{(c)} < D^{(l)} < D^{(s)} \quad (4.5)$$

$$b^{(s)} < b^{(l)} < b^{(c)} \quad (4.6)$$

are satisfied, a plot of the total inference time (I_t) versus bandwidth may appear similar to Figure 4.4. For some interval near zero bandwidth, the client-only strategy is to be preferred. However, as more bandwidth becomes available, the shared inference strategy begins to dominate. Then, as bandwidth further increases, the server-only strategy begins to dominate. Thus, there are regions of operation in which a particular strategy is preferable.

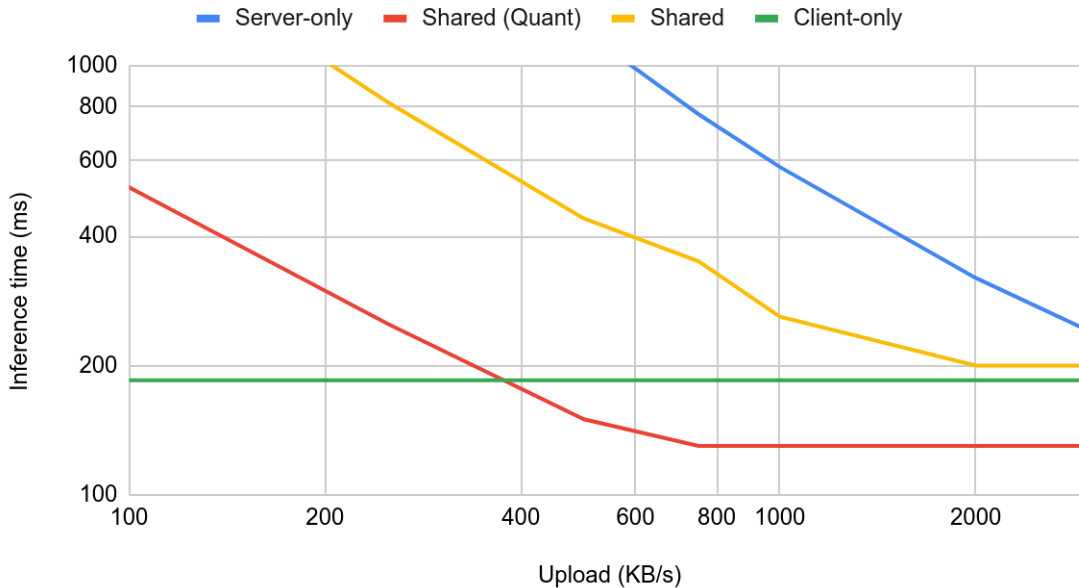


Figure 4.5: Total inference latency versus bandwidth. This data was collected using the prototype described in Section 4.1. The model under test is ResNet-34. The data transmitted in this experiment is uncompressed. The mobile client is a Samsung Galaxy S10 phone (Qualcomm Snapdragon 845) that is connected to the internet via a Wi-Fi network with a maximum available upload bandwidth of 3 MB/s. The server utilizes an NVIDIA GeForce GTX Titan X GPU. There is a distance of less than 5 km between the client and server, with an average ping time of 5 ms. To simulate different available bandwidths, the outgoing traffic is artificially rate limited within the client software itself.

This model of the latency is supported by experiments that were conducted on the prototype described in Section 4.1. Figure 4.5 shows how total inference time varies as the client’s upload bandwidth changes. Though the server-only inference has not reached a horizontal asymptote at the maximum bandwidth capacity, it is expected that it should continue to decrease until it reaches some value underneath the quantized shared inference curve.

As network conditions such as round trip time and bandwidth availability fluctuate, one can switch between different strategies to maintain a low total inference latency. In practice, one should apply hysteresis to the decision of switching between strategies. This is because switching models consumes time and energy as the models are loaded into memory. Furthermore, if network conditions are highly unstable, it is best to stick to a single model that reduces the average latency and also has a large enough region of operation for which the total inference latency is tolerable.

If one also considers the strategies for different split layers, it makes sense to pick a small subset of split layers that operate tolerably for a variety of network conditions. Since TensorFlow Lite client-side models must be stored individually in `.tflite` files, and — as of the time of this writing — since subgraphs cannot be extracted from a single trained model, it is important to restrict the

number of client-side models stored so that they don't consume unnecessary storage space on the mobile device.

4.3 Network protocol

To avoid congestion and improve flow control, TCP often makes use of Nagle's algorithm [27]. Nagle's algorithm forces the TCP socket to wait for an ACK response before transmitting more data. This introduces latency due to round-trip times. Thus, Nagle's algorithm should be disabled for large writes; instead, it is better to buffer the data when writing. One can set `TCP_NODELAY` on a Linux socket to disable Nagle's algorithm.

Instead of using TCP for transmission of tensor data, one could theoretically achieve lower latencies by using a custom protocol built on top of UDP. This would also allow the usage of custom error correction methods designed with compressed tensor data in mind.

A better real-time inference protocol design for minimizing inference latency and maximizing throughput should send maximally sized packets of tensor data, unless the end of a given tensor's serialized byte stream is reached. In that case, it should immediately flush the remaining contents of the send buffer and not wait for the send buffer to be filled. In pseudocode:

```
def process_send_buffer():
    if send_buffer.is_empty():
        return

    if send_buffer.size() >= mss:
        data = send_buffer.pop_bytes(mss)
        send(Packet(data))
        return

    if send_buffer.contains_end_of_tensor():
        data = send_buffer.pop_until_end_of_tensor()
        send(Packet(data))
```

where MSS (Maximum Segment Size) is the maximum amount of data that can be sent in a packet, excluding headers.

Another issue arises when the client attempts to send more requests than the server can process or that bandwidth of the connection can support. This phenomenon is often dubbed *backpressure*. To avoid backpressure, one needs to estimate expected server inference times as well as the available bandwidth of the connection. These estimates are to be utilized at the application layer of the Open System Interconnection (OSI) model to limit the client from sending requests when it is unwise to do so without increasing latencies or reducing overall throughput.

Server inference times can be tricky to determine if the server is handling multiple requests from different clients at once, particularly if the server implements batching to maximize throughput, or if the inference times are non-equal. A typical strategy is that the server manages its own time slicing and notifies its clients about their particular rate limits, which each client adheres to (and if a malicious client *doesn't* adhere to its given rate limits, hard limits can still be enforced server-side).

Because the available bandwidth is non-deterministic and varies over time, bandwidth limits can be tricky to estimate. One proposed method for developing a bandwidth estimation scheme involves the server sending confirmation upon the reception of a chunk of tensor data. Note that this confirmation does not necessarily correspond to “ACK”. If an out-of-order protocol such as UDP is used, the server should reply with a confirmation message containing information on the total number of bytes received, a unique identifier for the packet, and the time it is received at (assuming synchronized clocks). This helps the client’s bandwidth model account for out-of-order packets and potentially lost packets (for which it should also maintain some probabilistic model). By keeping a history of the confirmations, and also accounting for the additional latency introduced by the ping or round trip time (RTT), one can develop a real-time estimate of the bandwidth.

One simple strategy to avoid backpressure in the shared inference pipeline from the application layer of the OSI model is given as follows:

```
def send_request_to_server(request):
    while True:
        # Wait until server rate limit is satisfied.
        if now() < last_request_time + server_rate_limit:
            Thread.sleep(0)
            continue

        # Wait until we expect not to exceed bandwidth limits.
        if estimate_unreceived_bytes() > 0:
            Thread.sleep(0)
            continue

    write(request.data)
    break
```

For real-time processing of input frames, the aforementioned strategy is not sufficient: one needs to also account for client-side inference times. To minimize total inference latency, one strategy is to drop frames if the rate limiter can predict that any tensor data that is currently being sent to the network will not be flushed by the time the current frame completes preprocessing, client-side inference, and compression. This also reduces the wastage of client-side computational resources; frames no longer need to be dropped *after* spending time on client-side computation, only

to realize that there is no remaining bandwidth or server availability. An algorithm for real-time frame processing, optimized for latency, is given as follows:

```
def should_process_frame(frame):
    client_remain = estimate_client_process_latency()
    server_remain = last_request_time + server_rate_limit - now()
    bandwidth_remain = estimate_unreceived_bytes() / estimate_bandwidth()

    # Drop frame if server or bandwidth won't be available in time
    if (client_remain < server_remain or client_remain < bandwidth_remain):
        return False

    return True
```

Throughput (the total number of frames processed) can be further increased through a more advanced algorithm; however, any such algorithm will involve latency tradeoffs.

4.4 Library

To help aid in analysis and determining good split points, commonly needed functionality (splitting, inference, tiling, encoding, statistics) was extracted into a custom python module⁴ for collaborative intelligence. This section contains some usage examples.

Begin by importing relevant modules:

```
import collaborativeintelligence as ci
import numpy as np
from tensorflow import keras
```

Next, load the required model, and create the encoder and decoder layers, which will be attached to the end of the client model and beginning of the server model, respectively. For example, we can load a `keras.Model` from "filename.h5" and attach a simple uniform 8-bit quantization layer as the encoder layer:

```
model = keras.models.load_model("filename.h5")
encoder = ci.UniformQuantizationU8Encoder(clip_range=[-3., 3.])
decoder = ci.UniformQuantizationU8Decoder(clip_range=[-3., 3.])
```

To split the model:

⁴<https://github.com/YodaEmbedding/collaborative-intelligence/tree/master/src/lib>

```

model_client, model_server, _ = ci.split_model(
    model, layer=layer_name, encoder=encoder, decoder=decoder
)

```

Now, construct the postencoder and predecoder:

```

shape = model_client.output_shape[1:]
dtype = model_client.dtype
tensor_layout = ci.TensorLayout.from_shape(shape, "hwc", dtype)
postencoder = ci.JpegPostencoder(tensor_layout, quality=20)
tiled_layout = postencoder.tiled_layout
predecoder = ci.JpegPredecoder(tiled_layout, tensor_layout)

```

Finally, we may use the entire pipeline on a series of frames as follows⁵:

```

for frame in frames:
    x = frame
    x = model_client.predict(x[np.newaxis])[0]
    x = postencoder.run(x)
    x = predecoder.run(x)
    x = model_server.predict(x[np.newaxis])[0]
    print(x)

```

4.5 Summary

In this chapter, we discussed the technologies and design choices used in developing a proof-of-concept Android app, which was demoed at the NeurIPS 2019 conference. We established a concrete inference pipeline that took a real-time inference signal, preprocessed it, ran client-side inference, further compression-related tasks in “postencoder” separately from the deep model itself, sent the resulting data over the network, reassembled the data and fed it through a server-side “predecoder”, and finally ran the remaining deep model inference on the server.

Next, we established a model for assessing latency of various inference strategies using estimated hardware latencies and network conditions. We showed, in terms of inference latency, that certain strategies are optimal within certain intervals of available bandwidth. Of course, one may alternatively seek to optimize for a combination of other variables including throughput, energy usage, bandwidth costs, or data privacy — these will produce different characteristic curves.

⁵The single tensor `x` is put into a one-item batch preceding prediction via `x[np.newaxis]`. Then, we extract the first and only item from the predicted batch via `predict(...)[0]`. Here, we avoid collecting and batching more tensors because we are prioritizing low latency in lieu of throughput.

Next, we proposed a blueprint for a network protocol customized for transmitting real-time tensor streams. Though TCP is a reliable protocol for guaranteeing transmission of data, we can do better by building upon UDP in order to improve latency – particularly since exact and complete reception of tensor data is not necessary to perform a reasonably accurate inference, as was discussed in Section 3.2.

Finally, we briefly looked at some functionality provided by a library that was developed to help conduct experiments for this thesis, and also was used as part of the proof-of-concept server implementation.

Chapter 5

Conclusion

5.1 Thesis summary

Collaborative intelligence is a new concept for improving the mobile experience and bringing more powerful AI models to edge devices. This thesis looked to provide further insight into developing the shared inference strategy and provide pathways into developing practical applications that utilize this technique.

One of the core prerequisites towards making collaborative intelligence effective involves tensor data compression. In Section 1.1, we showed that information theory supports the idea that partial processing of a data tensor via non-generative feedforward networks reduces its entropy, and thus its theoretically minimum losslessly compressed size.

In Chapter 2, we looked at methods for improving this key requirement. By quantizing Batch-Norm layers or layers that follow batch normalized layers to as few as 6 quantization bins, one can often achieve near-equal Top-1 accuracies in image classification networks such as ResNet. This gave us a compression ratio of 12:1. To improve on this, we next looked at leveraging existing image codecs such as JPEG and JPEG 2000. These generated rate-accuracy curves that improved in shared inference accuracy for low rates as we split deeper into the model. For instance, at the `add_7` layer of ResNet-34, a compressed feature tensor size of 9 KB via JPEG resulted the same accuracy drop of 1% as a 15 KB JPEG compression of the $224 \times 224 \times 3$ input image.

In Chapter 3, we investigated the consequences of modifying and transforming values of the input and intermediate tensors. We discovered that we can minimize the drop in accuracy due to missing tensor data by filling in missing tensor entries with their precomputed mean value over a sample set of images. We also saw that as we apply common video-like transformations to the input data, such as the translation of an image, the feature tensor of a CNN responds in the same way. In fact, by precomputing the global motion vector between the reference input image and a translated input image, we can accurately predict the entries of their corresponding feature tensors to a high degree of accuracy by applying a downscaled version of the motion vector, where the tensor entries are interpolated if necessary. These ideas can be used to develop compression schemes for streams of tensors that result from a sequence of input data that contains temporal redundancies (e.g. video).

In Chapter 4, we took some of the concepts discussed in prior chapters and used them to develop an Android app and server for a working demonstration of collaborative intelligence. We also discussed possible extensions and improvements to this implementation, including a network protocol for real-time tensor streams. Finally, we looked at the range of available network bandwidths for which a shared inference strategy can perform better than a server-only or client-only inference strategy.

5.2 Future work

5.2.1 Model architecture

To expand the scope of collaborative intelligence, it is important to incorporate collaborative intelligence techniques with a larger number of existing models. One can also adapt and modify existing models to work better with these techniques by inserting new layers. For instance, the insertion of BatchNorm layers can be used to constrain the range of values and reduce the effect on inference accuracy due to lossy reconstructions. Encoder/decoder layers such as butterfly units [26] can also be useful in reducing tensor dimensionality. Training with compressible features has also been proposed [28]. Finally, more work needs to be done to design and introduce new model architectures that are specifically designed for collaborative intelligence, and exhibit the characteristics described in Section 1.2.

5.2.2 Tensor compression

Compression of feature tensors extracted from deep models is an active area of research [3], [29]–[32]. For CNN architectures, the primary concern is exploiting spatial (intraframe) and temporal (interframe) redundancies within a tensor stream that is generated from an input video stream. For this, it is useful to utilize existing video codecs for practical reasons such as reduced development effort, existing optimized implementations, and availability of hardware optimizations for operations used in encoding and decoding. Open source implementations (e.g. the x264 encoder for H.264) can be modified to assist the encoding process. Furthermore, one can also modify both the encoder *and* decoder to compress to a custom format which extends or modifies the original specification.

One possible modification makes use of the idea that we may reuse the same set of motion vectors across all the channels (as demonstrated in Section 3.1). However, the H.264 format requires us to store a copy of this set of motion vectors for each channel. To prevent this duplication from occurring, we must modify the encoder to store only one set of motion vectors in a custom H.264-like format, and the decoder to copy these motion vectors across all channels.

Furthermore, the typical coding block sizes are powers of 2, whereas channel dimensions may not be¹. Non-padded tiling of these channels makes it difficult to exploit the periodicity among the

¹In CNNs, channels are frequently sized at integer multiples of 7×7 .

channels that was noted in (2.6). DCT in particular produces different coefficients for phase shifted data. This deficiency needs to be addressed in order to achieve significantly lower bitrates.

5.2.3 Error concealment

There is often much spatially and temporally redundant information carried within tensor streams. Techniques like the ones mentioned in Section 3.2 use prior statistical knowledge, whereas tensor completion methods exploit more sophisticated spatial redundancies within tensors. However, there are also temporal redundancies that have not yet been considered. For instance, in real-time video transmission, one can fill in lost motion vectors using the motion vectors of previous frames. Similar or alternative techniques could also be developed for tensor streams.

5.2.4 Network protocol

As described in Section 4.3, a custom protocol for real-time transmission of compressed tensor streams would allow for lower latencies than the current reliable but slower TCP implementation. To deal with lost or corrupted packets, such a protocol could also implement error concealment methods designed specifically for tensor data.

5.2.5 Libraries

To make collaborative intelligence techniques easier to implement and design, and increase accessibility for non-experts, it is useful to have a set of libraries. These libraries can be utilized by both collaborative intelligence researchers as well as software developers of mobile apps and server back-ends, who may desire practical production grade solutions. Such libraries could contain tools for analyzing, developing, tuning, and deploying collaborative intelligence strategies. Useful features to consider include:

- backpressure-aware shared inference pipelines for real-time data processing
- combinators for methods used in tensor compression (e.g. quantization, tiling/weaving to convert between 3D and 2D tensor shapes, and interfacing with image/video/tensor codecs)
- implementation of a real-time tensor streaming protocol
- monitoring and collection of statistics for analysis
- real-time automated transitioning to optimal inference strategy based on network conditions
- simulations for assessing performance under different network conditions
- utilities for determination of good split points

References

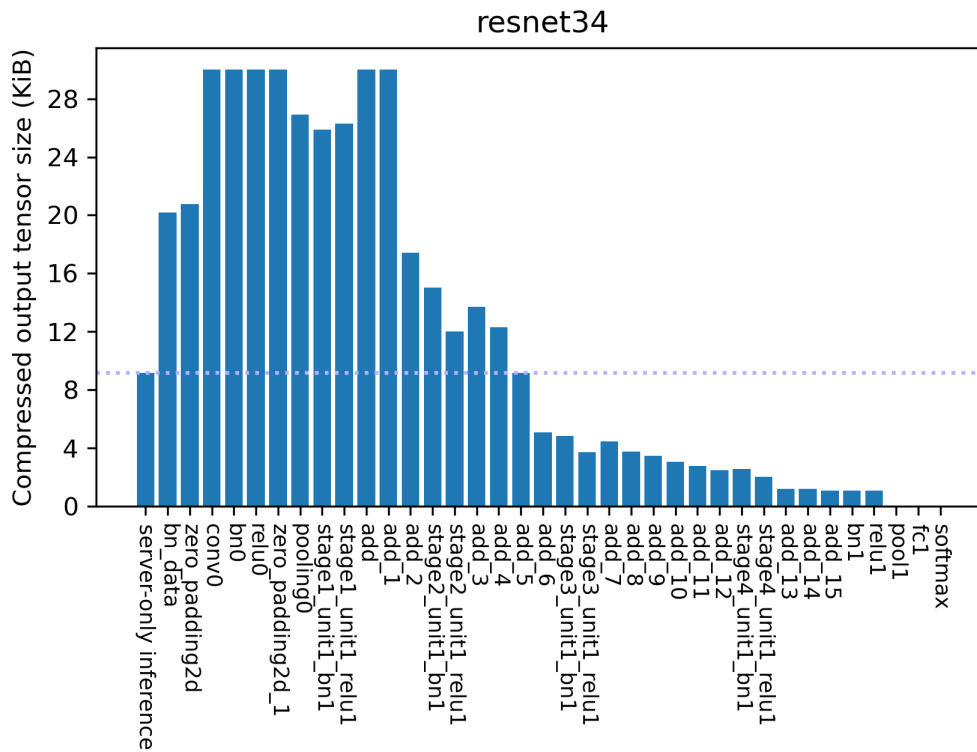
- [1] Y. Kang, J. Hauswald, C. Gao, *et al.*, “Neurosurgeon: Collaborative intelligence between the cloud and mobile edge,” *SIGARCH Comput. Archit. News*, vol. 45, no. 1, pp. 615–629, Apr. 2017, ISSN: 0163-5964. DOI: 10.1145/3093337.3037698. [Online]. Available: <https://doi.org/10.1145/3093337.3037698>.
- [2] A. E. Eshratifar, M. S. Abrishami, and M. Pedram, “JointDNN: An efficient training and inference engine for intelligent mobile cloud computing services,” *IEEE Transactions on Mobile Computing*, 2019, to appear.
- [3] H. Choi and I. V. Bajić, “Deep feature compression for collaborative object detection,” in *Proc. IEEE ICIP’18*, Oct. 2018, pp. 3743–3747. DOI: 10.1109/ICIP.2018.8451100.
- [4] T. M. Cover and J. A. Thomas, “Elements of Information Theory,” 2nd Edition. Wiley, 2006.
- [5] J. Zhang, T. Liu, and D. Tao, “An information-theoretic view for deep learning,” 2018. arXiv: 1804.09060 [stat.ML].
- [6] L. Weng, “Anatomize deep learning with information theory,” Sep. 28, 2017. [Online]. Available: <https://lilianweng.github.io/lil-log/2017/09/28/anatomize-deep-learning-with-information-theory.html>.
- [7] N. Tishby and N. Zaslavsky, “Deep learning and the information bottleneck principle,” 2015. arXiv: 1503.02406 [cs.LG].
- [8] K. Simonyan and A. Zisserman, “Very deep convolutional networks for large-scale image recognition,” in *Proc. ICLR*, 2015.
- [9] O. Ronneberger, P. Fischer, and T. Brox, “U-net: Convolutional networks for biomedical image segmentation,” in *Proc. MICCAI*, 2015.
- [10] K. He, X. Zhang, S. Ren, and J. Sun, “Deep residual learning for image recognition,” in *Proc. IEEE CVPR’16*, Jun. 2016, pp. 770–778. DOI: 10.1109/CVPR.2016.90.
- [11] M. Ulhaq and I. V. Bajić, “Shared mobile-cloud inference for collaborative intelligence,” NeurIPS’19 demo, 2020. arXiv: 2002.00157 [cs.AI].
- [12] S. Ioffe and C. Szegedy, “Batch normalization: Accelerating deep network training by reducing internal covariate shift,” 2015. arXiv: 1502.03167 [cs.LG].
- [13] S. Santurkar, D. Tsipras, A. Ilyas, and A. Madry, “How does batch normalization help optimization?” 2018. arXiv: 1805.11604 [stat.ML].
- [14] K. Sayood, “Introduction to Data Compression,” 5th Edition. Morgan Kaufmann, 2018.
- [15] O. Russakovsky, J. Deng, H. Su, *et al.*, “ImageNet Large Scale Visual Recognition Challenge,” *International Journal of Computer Vision (IJCV)*, vol. 115, no. 3, pp. 211–252, 2015. DOI: 10.1007/s11263-015-0816-y.

- [16] Independent JPEG Group, “Libjpeg,” version 9d, Jan. 12, 2020. [Online]. Available: <http://libjpeg.sourceforge.net>.
- [17] ITU-T, “Information technology – digital compression and coding of continuous-tone still images – requirements and guidelines,” International Telecommunication Union, Geneva, Recommendation T.81, Sep. 1992, p. 143.
- [18] J. D. Kornblum, “Using jpeg quantization tables to identify imagery processed by software,” *Digit. Investig.*, vol. 5, S21–S25, Sep. 2008, issn: 1742-2876. doi: 10.1016/j.diin.2008.05.004. [Online]. Available: <https://doi.org/10.1016/j.diin.2008.05.004>.
- [19] E. Kee, M. K. Johnson, and H. Farid, “Digital image authentication from jpeg headers,” *IEEE Transactions on Information Forensics and Security*, vol. 6, no. 3, pp. 1066–1075, 2011.
- [20] P. Yakubovskiy, “Image-classifiers,” version 1.0.0, Oct. 4, 2019. [Online]. Available: https://github.com/qubvel/classification_models.
- [21] D. Commander, “Libjpeg-turbo,” version 2.0.4, Dec. 31, 2019. [Online]. Available: <https://libjpeg-turbo.org>.
- [22] D. S. Taubman and M. W. Marcellin, “JPEG2000: Image Compression Fundamentals, Standards, and Practice.” Kluwer Academic Publishers, 2002.
- [23] U. d. L. Image and Signal Processing Group, “OpenJPEG,” version 2.3.1, Apr. 2, 2019. [Online]. Available: <https://www.openjpeg.org/>.
- [24] J. W. Woods, “Multidimensional Signal, Image, and Video Processing and Coding,” 2nd Edition. Elsevier - Academic Press, 2012.
- [25] L. Bragilevsky and I. V. Bajić, “Tensor completion methods for collaborative intelligence,” *IEEE Access*, vol. 8, pp. 41 162–41 174, 2020.
- [26] A. E. Eshratifar, A. Esmaili, and M. Pedram, “Towards collaborative intelligence friendly architectures for deep learning,” 2019. arXiv: 1902.00147 [cs.DC].
- [27] J. Nagle, “Congestion control in IP/TCP internetworks,” RFC Editor, RFC 896, Jan. 1984. [Online]. Available: <https://tools.ietf.org/html/rfc896>.
- [28] S. R. Alvar and I. V. Bajić, “Multi-task learning with compressible features for collaborative intelligence,” in *Proc. IEEE ICIP’19*, 2019, pp. 1705–1709.
- [29] H. Choi and I. V. Bajić, “Near-lossless deep feature compression for collaborative intelligence,” in *Proc. IEEE MMSP’18*, Aug. 2018, pp. 1–6. doi: 10.1109/MMSP.2018.8547134.
- [30] H. Choi, R. A. Cohen, and I. V. Bajić, “Back-and-forth prediction for deep tensor compression,” in *Proc. IEEE ICASSP’20*, 2020, pp. 4467–4471.
- [31] R. A. Cohen, H. Choi, and I. V. Bajić, “Lightweight compression of neural network feature tensors for collaborative intelligence,” in *Proc. IEEE ICME’20*, to appear, 2020.
- [32] Z. Chen, K. Fan, S. Wang, L. Duan, W. Lin, and A. C. Kot, “Toward intelligent sensing: Intermediate deep feature compression,” *IEEE Transactions on Image Processing*, vol. 29, pp. 2230–2243, 2020.

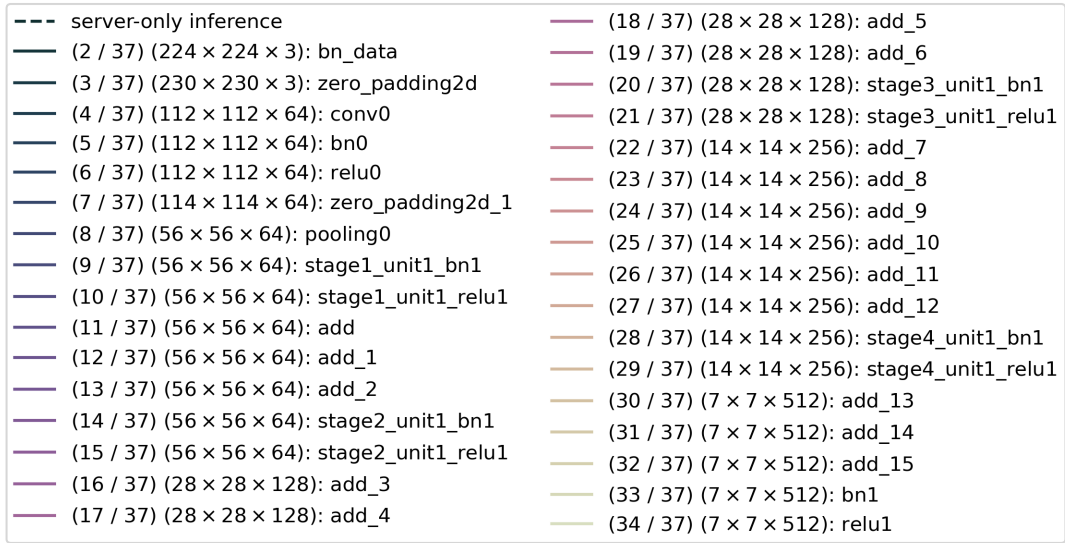
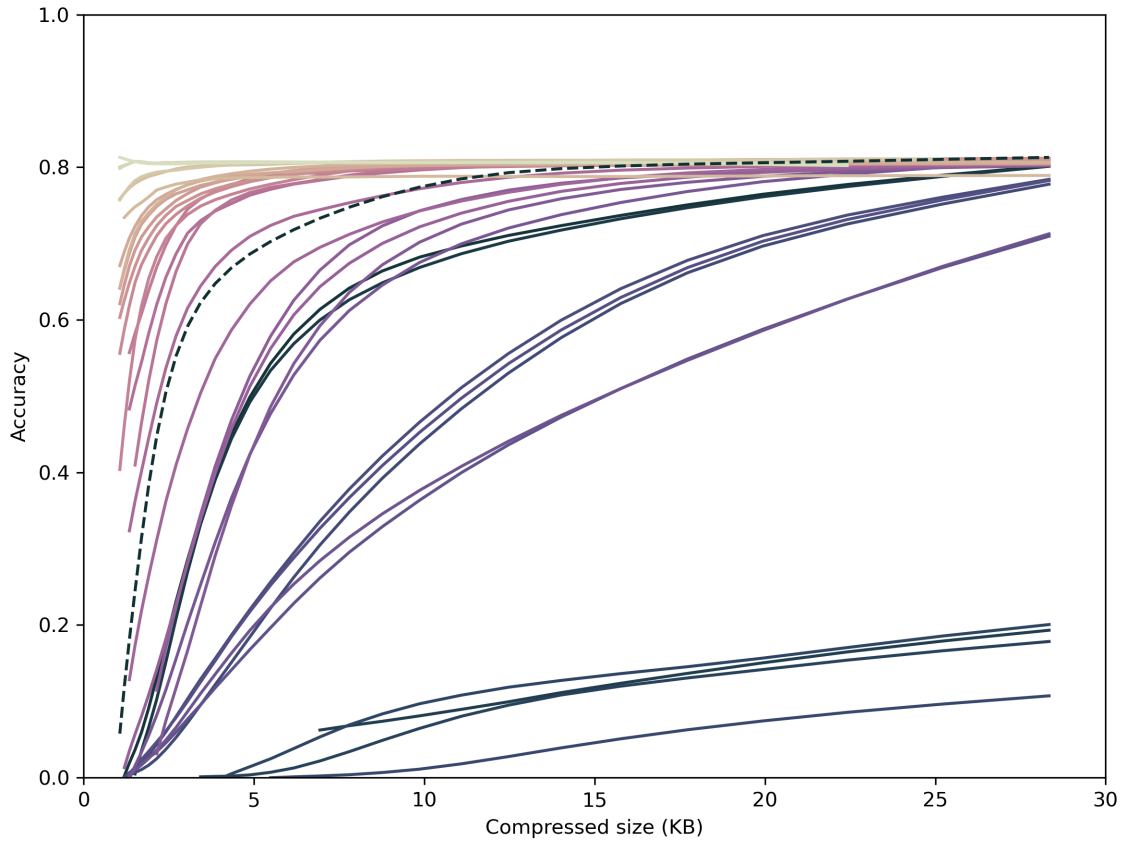
Appendix A

Additional figures

JPEG accuracy vs compressed output size (ResNet-34)



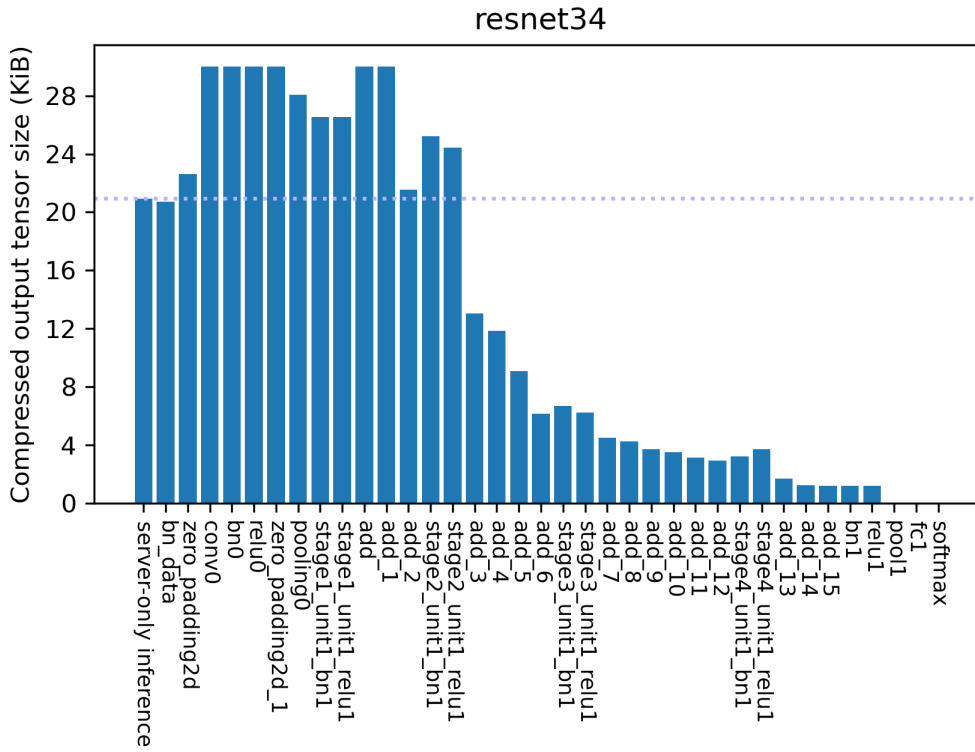
(a) compressed layer output size for < 5% drop in relative inference accuracy



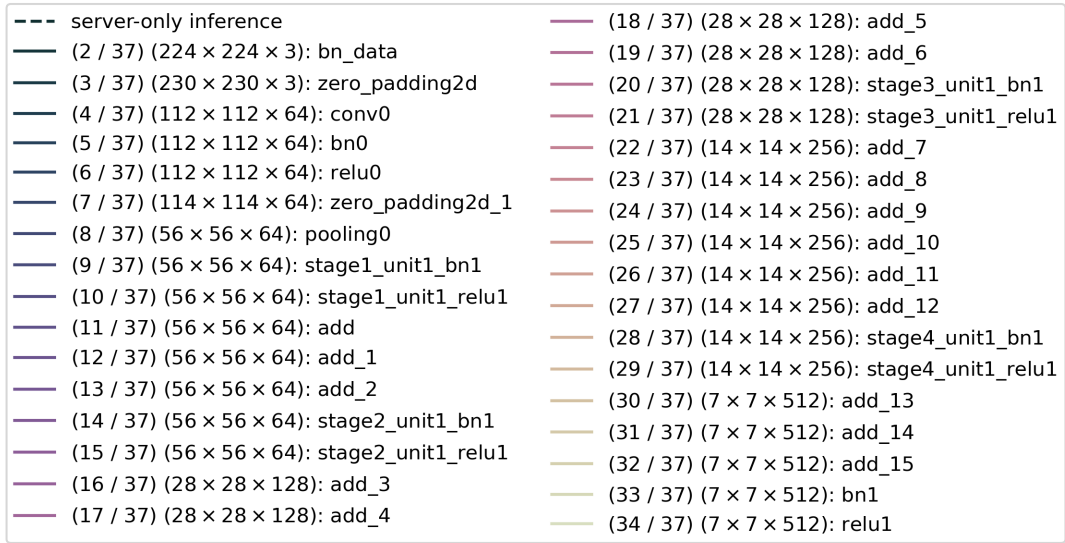
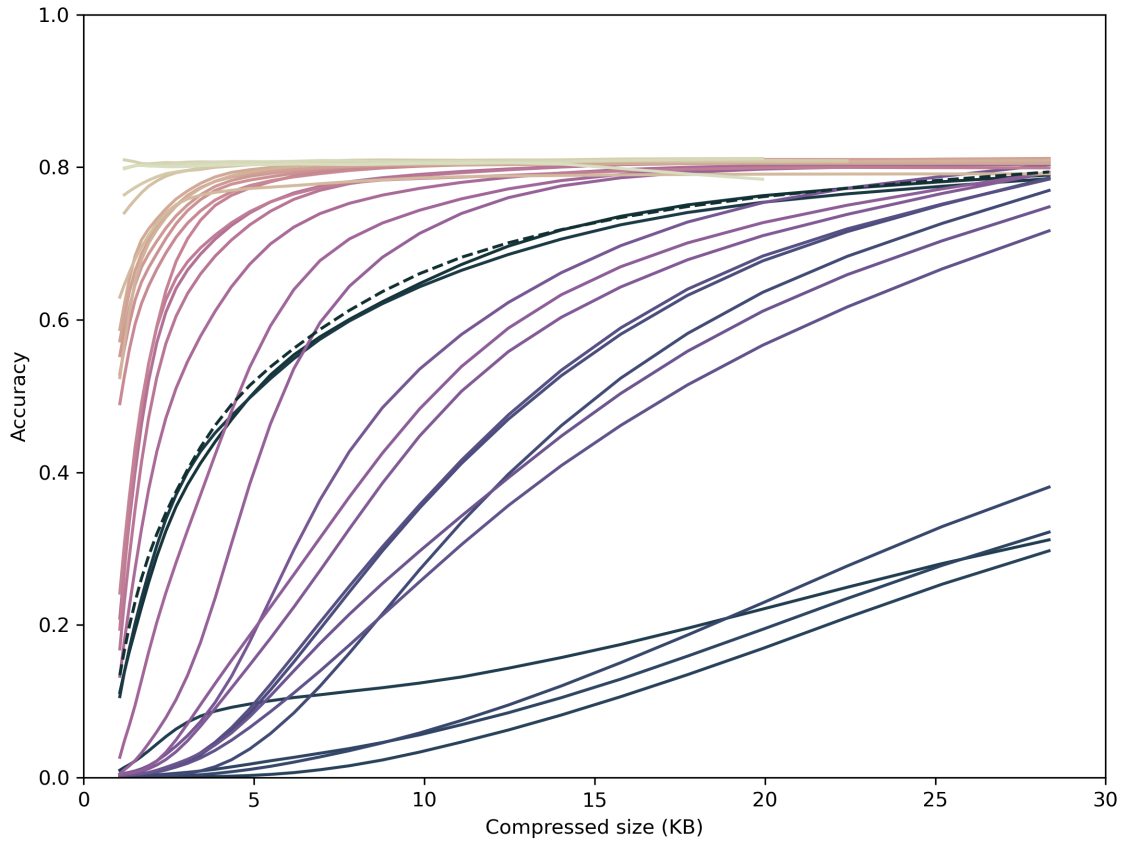
(b) curves for all layers, smoothing applied

Figure A.1: Top-1 image classification accuracy vs JPEG compressed frame output size across various layers of ResNet-34.

JPEG 2000 accuracy vs compressed output size (ResNet-34)



(a) compressed layer output size for < 5% drop in relative inference accuracy



(b) curves for all layers, smoothing applied

Figure A.2: Top-1 image classification accuracy vs JPEG 2000 compressed frame output size across various layers of ResNet-34.